FINITE ELEMENT SIM''LATION OF

CONTAMINATION TRANSPORT THROUGH AN AQUIFER

by

John B. Czarnecki

Submitted in Partial Fulfillment
of the Requirements for the Degree of
Master of Science in Hydrology

New Mexico Institute of Mining and Technology

Socorro, New Mexico

December, 1978

ABSTRACT

Two finite element formulations are presented based on hydraulic head-concentration and stream function-concentration models. Transient and steady-state cases are analyzed as well as the effect of concentration on viscosity. The hydraulic head-concentration formulation is incorporated into a computer code and the code is calibrated by running a previously solved sea water intrusion problem. The model is then used to solve hypothetical one- and two-dimensional contaminant transport problems using irregular and regular meshes. A discussion of the effect of Peclet and Courant numbers on oscillation is included.

CONTENTS

FIGURES

TABLES

1. Introduction

1.1. General

The problem of contamination transport through an aquifer by
the movement of ground water is of major interest to hydrologists and
has been analyzed in various ways for several years now. The equations
governing the movement of ground water and the transport of a contami-
nant are of such a nature that analytical solutions can only be obtain-
ed for idealized one- and two-dimensional problems. To deal with more
realistic flow situations, it is necessary to obtain approximate sol-
utions via the use of numerical schemes such as the finite difference
or finite element methods. These governing equations are not restrict-
ed in their application to ground water flow and "pollutant" transport
problems; with a slight twist in the interpretation of a few parameters
present in these equations, it is possible to apply them toward problems
involving geothermal flow, where the "pollutant", instead of being
an undesirable or toxic substance, is temperature.

It is from this framework that the work presented in this thesis
is derived. A portion of the work presented here is a part of a
geothermal modeling study at New Mexico Institute of Mining and Tech-
nology, the aim of which is to formulate an effective model to simulate
geothermal flow in an area west of Socorro, New Mexico, using the
finite element technique.

1.2 Purpose and scope

The purpose of this thesis is to develop an effective numerical
model which will solve transport problems in two dimensions using
the finite element method. Since the development of any new model

necessitates some form of calibration, and since this model is designed
to solve problems involving contaminant transport as well as geothermal
flow (due to the generality of the governing equations), a calibration
problem involving sea water intrusion has been run and the results are
reported within the thesis.

As a demonstration of how this model could be applied to an actual
aquifer situation, a problem was devised involving one-dimensional
and two-dimensional flow within the Rustler Formation of the Los Medanos
Area near Carlsbad, New Mexico. Since many of the parameters used in
the transport analysis are at best rough estimates or guesses, the
results obtained must be considered as hypothetical. The purpose of
using the model in this manner is not to supply definitive answers
for the "actual" transport problems analyzed; rather, these problems
have been used to test the effectiveness of the model and to identify
possible numerical difficulties within the model, such as oscillations,
which may occur for certain sets of values of some of the parameters
used.

1.3. Literature review

Various numerical schemes have been proposed by several workers
to solve problems involving contaminant transport or geothermal flow.
Among the more currently developed transport schemes are the material
transport finite element Galerkin model of Duguid and Reeves[4]; the
coupled ground water flow and convective dispersion finite element
model of Huyakorn and Taylor[7]; the three-dimensional convective disper-
sion finite element model of Taylor and Huyakorn[13]; and the transient
transport, upstream weighted, finite element model of Huyakorn and

Nilkuha[6]. Work done in the area of geothermal flow includes the convective heat transfer model of Domenico and Palciauskas and the numerical analysis of Witherspoon et al[14].

The numerical model used in this thesis incorporates the upstream weighting procedure of Huyakorn[5]. The advantage of using upstream weighting becomes apparent when numerical oscillation problems are encountered. In addition, this model features a sequential iterative solution scheme which treats the governing equations as being uncoupled, thus reducing the size of the coefficient matrix and hence the required computational time.

2. Formulation of Coupled Ground Water Flow and Convective Dispersion Equations

2.1. General

The transport of a contaminant by the movement of ground water can be simulated using three different models: (1) velocities-pressure-concentration model; (2) hydraulic head-concentration model; and (3) stream function-concentration model (Huyakorn and Taylor, 1977, p. 1.131). The latter two models lend themselves more readily to computer simulation than the first since they have fewer variables to calculate. For this reason, the latter two models have been used in this thesis and appear in the following sections.

2.2. Hydraulic head--concentration (h-c) formulation

2.2.1. Governing equations

The equations describing coupled steady ground water flow and contamination transport may be written in the form

$$v_i = - \frac{k_{ij} \rho\, g}{\mu\, n} \left(\frac{1}{\rho g} \frac{\partial p}{\partial x_i} + e_i \right) \tag{1}$$

$$\frac{\partial}{\partial x_i} \left(\rho v_i \right) = 0 \tag{2}$$

$$\frac{\partial}{\partial x_i} \left(D_{ij} \frac{\partial c}{\partial x_j} \right) - v_i \frac{\partial c}{\partial x_i} = \lambda \frac{\partial c}{\partial t} \tag{3}$$

where v_i denotes the components of the seepage velocity (L/T); k_{ij}

is the intrinsic permeability tensor of the porous medium (L^2); μ is the dynamic viscosity of the fluid (M/LT); ρ is the fluid density (M/L^3); g is the gravitational acceleration (L/T^2); p is the fluid pressure (M/LT^2); e_i denotes the components of the unit vector in the upward vertical direction; D_{ij} is the dispersion tensor (L^2/T); c is the concentration of pollutant, in this case salt (M/L^3); λ is the concentration coefficient which is set equal to unity; and n is the effective porosity of the porous medium. Eqs. (2) and (3) are referred to as the continuity and convective dispersion equations respectively (Bear, 1972, pp. 617, 645).

Fluid density and salt concentration are related by

$$\rho = \rho_0 + (\rho_1 - \rho_0)\ c/c_1 \qquad (4a)$$

where ρ_o is a reference density at a reference concentration, c_o, usually taken to be zero; ρ_1 denotes density at a maximum concentration, c_1 (i.e. the highest concentration).

Assuming the dominant solute present to be sodium chloride, data provided form Table 1 can be used in determining the weighted, least square, fitted curve equation relating concentration and viscosity, by using a computer code entitled CRVFIT (Appendix I). Thus, the relation between relative fluid viscosity and NaCl concentration, in grams per liter, at $25^{\circ}C$ is computed as

$$\mu/\mu_o = 1 + Ac + Bc^2$$
$$= 1 + 1.46 \times 10^{-3}\ c + 3.1 \times 10^{-6}\ c^2 \quad (4b)$$

where the units of A and B are liters/grams and $(\text{liters/grams})^2$

Table 1 Data relating relative fluid viscosity to sodium chloride concentration (International Critical Tables, 1929, p.15).

Sodium Chloride Concentration per 1000 grams water, c		Relative Viscosity μ/μ_0			Viscosity Difference between 60° and 10° data	
Formula Weight	Grams	@10°C	@25°C	@60°C		
0.1	5.8	1.006	1.009	1.012	0.006	(0.6%)
0.25	14.6	1.016	1.022	1.030	0.018	(1.4%)
0.5	29.2	1.032	1.046	1.060	0.028	(2.7%)
1.0	58.4	1.071	1.094	1.121	0.050	(4.7%)
2.0	116.8	1.173	1.205	1.249	0.076	(6.5%)
3.0	175.2	1.312	1.341	1.39	0.078	(5.9%)
4.0	233.6	1.481	1.509	1.54	0.059	(4.0%)
5.0	292.0	1.692	1.706	1.72	0.028	(1.7%)

Note: 1 formula weight of NaCl = 58.4 grams.
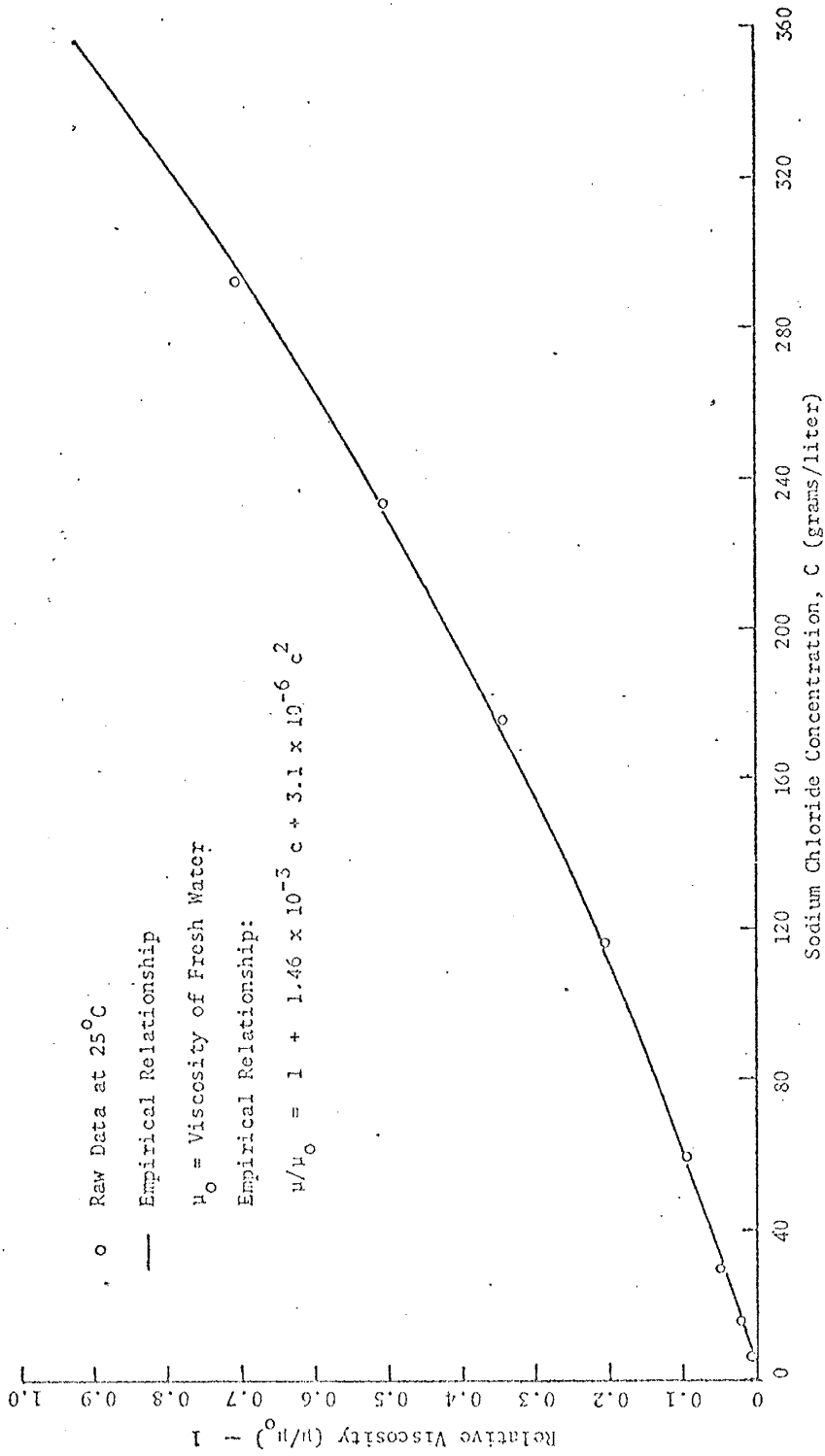
Fig. 1 Plot of relative viscosity $(\mu/\mu_o) - 1$ versus sodium chloride concentration in grams/liter for solutions at 25°C.

o   Raw Data at 25°C

———   Empirical Relationship

μ_o = Viscosity of Fresh Water

Empirical Relationship:

$$\mu/\mu_o = 1 + 1.46 \times 10^{-3} \, c + 3.1 \times 10^{-6} \, c^2$$

Sodium Chloride Concentration, C (grams/liter)

Relative Viscosity $(\mu/\mu_o) - 1$

Relative Viscosity $(\mu/\mu_0) - 1$

Sodium Chloride Concentration, C (grams/liter)

10°C

60°C
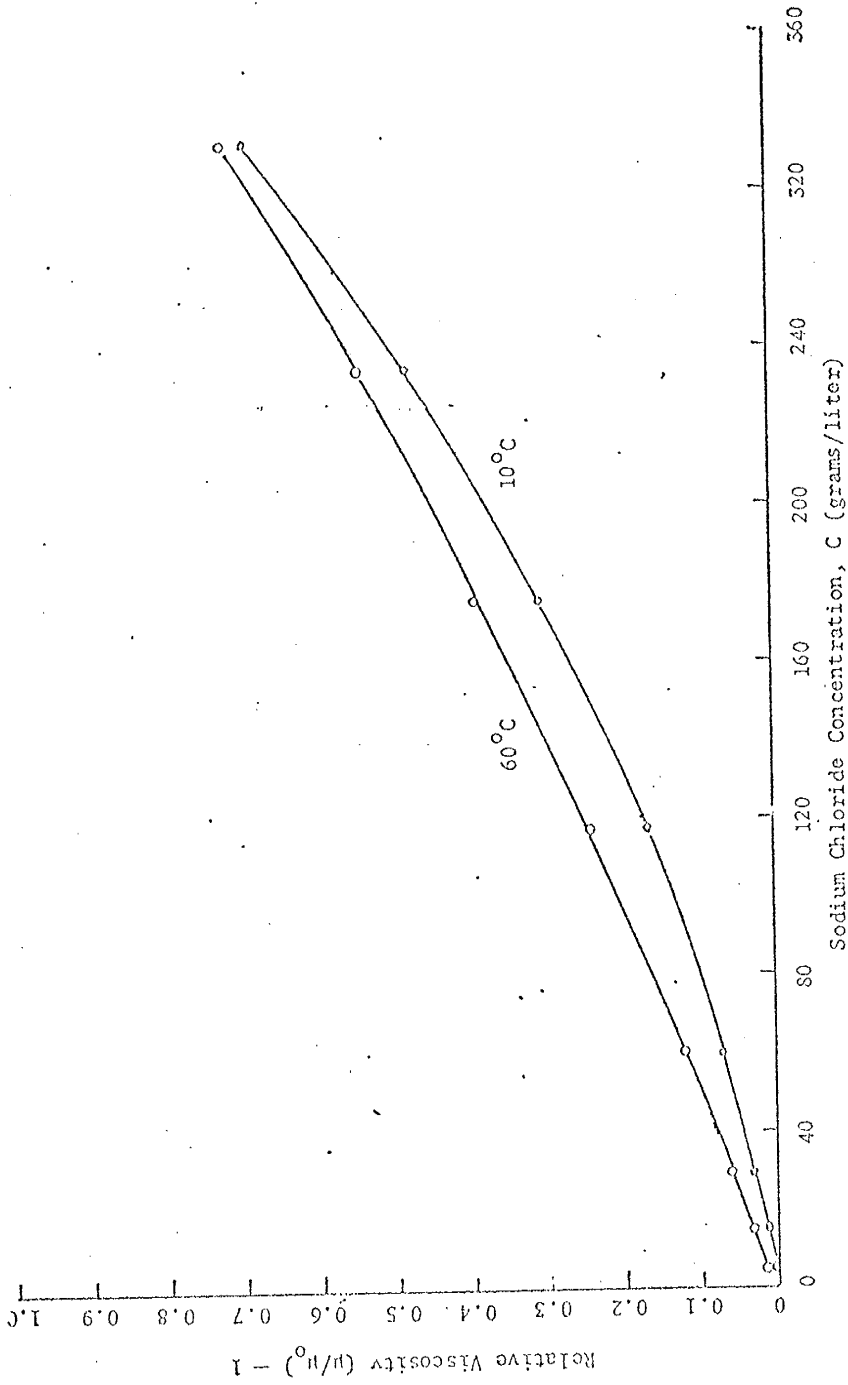
Fig. 2   Plot showing the effect of temperature on relative viscosity versus salt concentration

for NaCl solutions at 10°C and 60°C.

respectively.

In order to show the effect of temperature on relative viscosity as a function of NaCl concentration, data for two temperature extremes (10°C and 60°C) have been plotted in Fig. 2. Referring to Table 1, a maximum difference in relative viscosity occurs at a concentration of 116.8 grams which can be expressed in terms of a percent difference as 6.5%. Since this maximum difference is small it is sufficient to allow eq. (4b) to serve as the emperical relation between relative fluid viscosity and NaCl concentration for the entire expected range of temperatures. Additional viscosity data for a wide range of NaCl concentrations at 20°C is in close agreement with the values presented in Table 1 (CRC Handbook of Chemistry and Physics, 1974, pp. D-224-- D-225).

In working with the flow equation, it is more convenient to replace pressure by the reference hydraulic head which is defined as

$$h = \frac{p}{\rho_o g} + z \tag{5}$$

where z is the elevation above a selected datum plane. Taking the partial derivative of eq. (5) with respect to x_i amd rearranging, one obtains

$$\frac{\partial p}{\partial x_i} = \rho_o g \left(\frac{\partial h}{\partial x_i} - \frac{\partial z}{\partial x_i} \right)$$

$$= \rho_o g \left(\frac{\partial h}{\partial x_i} - e_i \right) \tag{6}$$

Eq. (6) can now be substituted into eq. (1) to yield

$$v_i = - \frac{k_{ij} \, \rho g}{\mu \, n} \left[\frac{\rho_o}{\rho} \left(\frac{\partial h}{\partial x_i} - e_i \right) + e_i \right] \tag{7}$$

which upon rearrangement becomes

$$v_i = - \frac{k_{ij} \rho_o g}{\mu_o n} \frac{\mu_o}{\mu} \left[\left(\frac{\partial h}{\partial x_i} - e_i \right) + \frac{\rho}{\rho_o} e_i \right]$$

$$= - (K_{ij})_o \frac{\mu_o}{\mu} \left[\frac{\partial h}{\partial x_i} + \frac{(\rho - \rho_o)}{\rho} e_i \right] \tag{8}$$

where $(K_{ij})_o$ is the reference hydraulic conductivity tensor defined as $(K_{ij})_o = K_{ij} \rho_o g / (\mu_o n)$.

Substituting eq. (4a) into (8) yields

$$v_i = - (K_{ij})_o \frac{\mu_o}{\mu} \left[\frac{\partial h}{\partial x_i} + \frac{(\rho_1 - \rho_o) c}{\rho_o c_1} e_i \right] \tag{9}$$

For isotropic porous media, eq. (9) reduces to

$$v_i = - K_o \frac{\mu_o}{\mu} \left[\frac{\partial h}{\partial x_i} + \varepsilon \frac{c}{c_1} e_i \right] \tag{10}$$

where $\varepsilon = (\rho_1 - \rho_o)/\rho_o$. Substituting eq. (10) into (2), we obtain

$$\frac{\partial}{\partial x_i} \left[\rho K_o \frac{\mu_o}{\mu} \varepsilon \frac{c}{c_1} e_i \right] + \frac{\partial}{\partial x_i} \left[\rho K_o \frac{\mu_o}{\mu} \frac{\partial h}{\partial x_i} \right] = 0 \tag{11}$$

If, as a matter of convenience, an isotropic dispersion tensor is assumed, then the transport equation reduces to

$$\frac{\partial}{\partial x_i} \left(D \frac{\partial c}{\partial x_i} \right) - v_i \frac{\partial c}{\partial x_i} = \frac{\partial c}{\partial t} \tag{12}$$

Strictly speaking, however, the dispersion tensor will not be isotropic since it depends on the longitudinal and transverse dispersivities which are not necessarily equal. The governing equations for this problem then are represented by Eqs. (4a), (10), (11), and (12).

2.2.2. Reduction of equations to dimensionless form

A better understanding of coupled groundwater flow and convective dispersion may be obtained via dimensional analysis. To reduce the governing differential equations to dimensionless form, the following set of dimensionless variables and parameters are introduced:

$$x_i^* = x_i/d; \qquad v_i^* = v_i/V; \qquad \frac{\partial}{\partial x_i} = \frac{1}{d} \frac{\partial}{\partial x_i^*}; \tag{13}$$

$$h^* = h/d; \quad c^* = c/c_1; \quad t^* = \frac{D_o t}{d^2}; \quad \frac{\partial}{\partial t} = \frac{D_o}{d^2} \frac{\partial}{\partial t^*}; \tag{14}$$

$$\mu^* = \mu/\mu_o; \quad \rho^* = \rho/\rho_o; \quad D^* = D/D_o; \quad \varepsilon = (\rho_1 - \rho_o)/\rho_o; \tag{15}$$

where d is the characteristic length of the flow system; V is the characteristic velocity; D_o is the characteristic dispersion coefficient of the porous medium; and μ_o is the dynamic viscosity of the fluid at the reference concentration.

Eq. (10) can be non-dimensionalized by making the following substitutions: substituting eq. (13) into eq. (10) gives

$$v^*_i = - \frac{K_o}{V} \frac{\mu_o}{\mu} \left[\frac{1}{d} \frac{\partial h}{\partial x^*_i} + \frac{(\rho_1 - \rho_o)}{\rho_o} \frac{c}{c_1} e_i \right] \qquad (16)$$

Substituting eqs. (14) and (15) into eq. (16) yields

$$v^*_i = - \frac{K_o}{V\mu^*} \left[\frac{\partial h^*}{\partial x^*_i} + \varepsilon\, c^* e_i \right] \qquad (17)$$

which when substituted into eq. (11) yields

$$\frac{\partial}{\partial x^*_i} \left[\frac{\rho^*}{\mu^*} \frac{\rho_o K_o}{d} \frac{\partial h^*}{\partial x^*_i} \right] + \frac{\partial}{\partial x^*_i} \left[\frac{\rho^*}{\mu^*} \frac{\rho_o K_o}{d} \varepsilon c^* \right] e_i = 0 \qquad (18)$$

Since ρ_o, K_o, and d are constants, we can write eq. (18) as

$$\frac{\rho_o K_o}{d} \left[\frac{\partial}{\partial x^*_i} \left(\frac{\rho^*}{\mu^*} \frac{\partial h^*}{\partial x^*_i} \right) + \frac{\partial}{\partial x^*_i} \left(\frac{\rho^*}{\mu^*} \varepsilon\, c^* \right) e_i \right] = 0 \qquad (19)$$

Eq. (19) may be expressed in the form

$$\frac{K_o}{V} \left[\frac{\partial}{\partial x^*_i} \left(\frac{\rho^*}{\mu^*} \frac{\partial h^*}{\partial x^*_i} \right) + \frac{\partial}{\partial x^*_i} \left(\frac{\rho^*}{\mu^*} \varepsilon c^* \right) e_i \right] = 0 \qquad (20)$$

Eq. (12) can be non-dimensionalized as follows: substituting eq. (13) into eq. (12) yields

$$\frac{1}{d} \frac{\partial}{\partial x^*_i} \left[D \frac{1}{d} \frac{\partial c}{\partial x^*_i} \right] - \frac{v^*_i V}{d} \frac{\partial c}{\partial x^*_i} = \frac{\partial c}{\partial t} \qquad (21)$$

Substituting eqs. (14) and (15) into (21) yields

$$\frac{1}{d}\frac{\partial}{\partial x_i^*}\left[\frac{D^* D_o c_1}{d}\frac{\partial c}{\partial x_i^*}\right] - \frac{v_i^* V}{d}c_1\frac{\partial c^*}{\partial x_i^*} = \frac{D_o}{d^2}c_1\frac{\partial c^*}{\partial t^*} \qquad (22)$$

Since the quantities d, D_o, and c_1 are constants, they can be brought outside the parentheses. Eq. (22) can be simplified to give

$$\frac{\partial}{\partial x_i^*}\left(D^*\frac{\partial c^*}{\partial x_i^*}\right) = \frac{Vd}{D_o}v_i^*\frac{\partial c^*}{\partial x_i^*} + \frac{\partial c^*}{\partial t^*} \qquad (23)$$

where the dimensionless parameter Vd/D_o is referred to as the Peclet number. Finally, eq. (4) may be made dimensionless. Substituting eq. (14) into eq. (4) yields

$$\rho = 1 + [(\rho_1 - \rho_o)/\rho_1]c^* \qquad (24)$$

Substituting eq. (15) into eq. (24) gives

$$\rho^* = 1 + \varepsilon\, c^* \qquad (25)$$

where ε is refered to as the "density difference ratio". Eqs. (17), (20), (23), and (25) form the set of governing equations in dimensionless form.

2.2.3. Application of the Galerkin finite element method

The Galerkin finite element method will be applied to the dimensional governing equations, i.e. eqs. (11) and (12). To apply this method,

trial solutions for hydraulic head and concentration are introduced as

$$\hat{h} = N_I(x_i)h_I(t) \tag{26a}$$

$$\hat{c} = N_I(x_i)c_I(t) \tag{26b}$$

The Galerkin criterion (Pinder and Gray, 1977, p. 57) requires that

$$\int_R N_I \left[\frac{\partial}{\partial x_i}\left(\rho K_o \frac{\mu_o}{\mu} \varepsilon \frac{\hat{c}}{c_1} e_i \right) + \frac{\partial}{\partial x_i}\left(\rho \frac{K_o \mu_o}{\mu} \frac{\partial \hat{h}}{\partial x_i} \right) \right] dR = 0 \tag{27}$$

and

$$\int_R N_I \left[\frac{\partial}{\partial x_i}\left(D \frac{\partial \hat{c}}{\partial x_i} \right) - v_i \frac{\partial \hat{c}}{\partial x_i} - \frac{\partial \hat{c}}{\partial t} \right] dR = 0 \tag{28}$$

After applying Green's theorem and substituting for $\hat{h}$ and $\hat{c}$, eq. (27) becomes

$$\int_B N_I \left[\rho K_o \frac{\mu_o}{\mu}\left(\varepsilon \frac{\hat{c}}{c_1} e_i + \frac{\partial \hat{h}}{\partial x_i} \right) n_i \right] dB$$

$$- \int_R \left[\rho \frac{K_o \mu_o}{c_1 \mu} \varepsilon \frac{\partial N_I}{\partial x_i} N_J\, c_J\, e_i + \rho \frac{K_o \mu_o}{\mu} \frac{\partial N_I}{\partial x_i} \frac{\partial N_J}{\partial x_i} h_J \right] dR = 0 \tag{29}$$

Making use of the relation

$$v_i = - \frac{K_o \mu_o}{\mu} \left[\frac{\partial \hat{h}}{\partial x_i} + \varepsilon \frac{\hat{c}}{c_1} e_i \right] \tag{30a}$$

and incorporating the fluid flux boundary condition

$$v_i n_i = -q \qquad \text{on } B_2, \qquad (30b)$$

eq. (29) becomes

$$\left[\int_R \rho \, \frac{K_o \mu_o}{c_1 \mu} \, \varepsilon \, \frac{\partial N_I}{\partial x_i} \, N_J \, e_i \, dR \right] c_J + \left[\int_R \frac{K_o \mu_o}{\mu} \, \rho \, \frac{\partial N_I}{\partial x_i} \, \frac{\partial N_J}{\partial x_i} \, dR \right] h_J$$

$$= \int_{B_2} N_I \rho \, q \, dB \qquad (31)$$

It should be understood that the hydraulic head condition on B_1 is prescribed.

Similarly, application of Green's theorem to the second order derivative term of eq. (28) leads to

$$\int_B N_I D \, \frac{\partial \hat{c}}{\partial x_i} \, n_i \, dB - \left[\int_R \left(D \, \frac{\partial N_I}{\partial x_i} \, \frac{\partial N_J}{\partial x_i} + v_i \, N_I \, \frac{\partial N_J}{\partial x_i} \right) dR \right] c_J$$

$$- \int_R N_I N_J \, \frac{dc_J}{dt} \, dR = 0 \qquad (32)$$

Incorporating the boundary condition

$$D \, \frac{\partial \hat{c}}{\partial x_i} \, n_i = Q \qquad \text{on } B_2' \qquad (33)$$

where Q is the concentration flux on B_2'; and assuming that concentration is prescribed on B_1', eq. (32) becomes

$$
\left[\int_R \left(D \, \frac{\partial N_I}{\partial x_i} \, \frac{\partial N_J}{\partial x_i} + v_i N_I \, \frac{\partial N_J}{\partial x_i} \right) dR \right] c_J + \int_R N_I N_J \, \frac{dc}{dt} J \, dR
$$

$$
= \int_{B_2'} N_I Q dB \tag{34}
$$

For a steady state case, eq. (34) reduces to

$$
\left[\int_R \left(D \, \frac{\partial N_I}{\partial x_i} \, \frac{\partial N_J}{\partial x_i} + v_i N_I \, \frac{\partial N_J}{\partial x_i} \right) dR \right] c_J = \int_{B_2'} N_I \, Q \, dB \tag{35}
$$

2.2.4. Solution procedure

A. Steady-state case: For steady-state conditions, eqs. (31) and (35) can be solved independently. Eqs. (31) and (35) can be written in matrix form as

$$
[A]\{h\} = \{R\} \tag{36a}
$$

$$
[G]\{c\} = \{F\} \tag{36b}
$$

where

$$
A_{IJ} = \sum_e \int_{R^e} \frac{K_o \mu_o}{\mu} \, \rho \, \frac{\partial N_I}{\partial x_i} \, \frac{\partial N_J}{\partial x_i} \, dR = \sum_e \int_{R^e} K \, \rho_o \, \frac{\partial N_I}{\partial x_i} \, \frac{\partial N_J}{\partial x_i} \, dR \tag{37a}
$$

$$R_I = \sum_e \left[- \int_{R^e} \rho \frac{K_o \mu_o}{\mu} \varepsilon \frac{\partial N_I}{\partial x_i} \frac{\hat{c}}{c_1} e_i \, dR + \int_{B_2^e} N_I \rho q \, dB \right] \qquad (37b)$$

$$G_{IJ} = \sum_e \int_{R^e} \left(D \frac{\partial N_I}{\partial x_i} \frac{\partial N_J}{\partial x_i} + v_i N_I \frac{\partial N_J}{\partial x_i} \right) dR \qquad (37c)$$

$$F_I = \sum_e \int_{B_2^{'e}} N_I Q \, dB \qquad (37d)$$

The solution scheme begins by solving the flow equation (36a) by assuming an initial set of concentrations and taking account of the symmetric nature of the coefficient matrix. Having obtained hydraulic head values, velocities are calculated and fed into the convective dispersion equation (36a) which is solved using an asymmetric equation solver. Iteration is performed until satisfactory convergence is achieved.

As an alternative, eqs. (31) and (35) can be solved simultaneously. Combining these two equations in matrix notation yields

$$[H]\{\Phi\} = \{E\} \qquad (38)$$

where the typical matrix elements are given as

$$[H_{IJ}] = \begin{bmatrix} a_{IJ} & b_{IJ} \\ 0 & d_{IJ} \end{bmatrix} \qquad (39a)$$

$$\{\Phi_J\} = \begin{Bmatrix} h_J \\ c_J \end{Bmatrix} ; \qquad \{E_I\} = \begin{Bmatrix} E_{I1} \\ E_{I2} \end{Bmatrix} ; \qquad (39b)$$

and

$$a_{IJ} = \sum_e \int_{R^e} \rho \frac{K_o \mu_o}{\mu} \frac{\partial N_I}{\partial x_i} \frac{\partial N_J}{\partial x_j} \, dR \tag{40a}$$

$$b_{IJ} = \sum_e \int_{R^e} \rho \frac{K_o \mu_o}{c_1 \mu} \varepsilon \frac{\partial N_I}{\partial x_i} N_J \, e_i \, dR \tag{40b}$$

$$d_{IJ} = \sum_e \int_{R^e} \left(D \frac{\partial N_I}{\partial x_i} \frac{\partial N_J}{\partial x_i} + v_i N_I \frac{\partial N_J}{\partial x_i} \right) dR \tag{40c}$$

$$E_{I1} = \sum_e \int_{B_2^e} N_I \, \rho \, q \, dB \tag{40d}$$

$$E_{I2} = \sum_e \int_{B_2'^e} N_I \, Q \, dB \tag{40e}$$

The coupled solution algorithm begins with the formation of the co-efficient matrix [A] using a starting set of values for hydraulic head. Iteration is performed until satisfactory convergence is achieved.

B. Transient case: Eqs. (31) and (34) form the required set of nonlinear governing equations for the transient case. It is possible, as in the above solution procedure, to solve the flow equation, eq. (31), by assuming an initial set of concentration values, which leads to a so-lution set of hydraulic head values. These hydraulic head values in turn, together with an initial guess of concentration values, are used in eq. (30a) to obtain the required velocity values for eq. (34). These values

of velocity are used in eq. (34) to obtain the nodal concentrations. Iteration of the above procedure is performed within each time step until the differences between successive iterates of hydraulic head and concentration converge to prescribed tolerances. From the viewpoint of computational time, it is more advantageous to solve the two equations sequentially rather than coupled. In a case where convergence difficulties are encountered, the time step size may be reduced to circumvent the problem.

Since eq. (34) contains the time derivative, we employ finite differences to perform integration with respect to time. Prior to employing this method, it is convenient to write eq. (34) in matrix form as

$$[G]\{c\} + [M]\left\{\frac{dc}{dt}\right\} = \{F\} \tag{41}$$

where

$$G_{IJ} = \sum_{e} \int_{R^e} \left(D \frac{\partial N_I}{\partial x_i} \frac{\partial N_J}{\partial x_i} + v_i N_I \frac{\partial N_J}{\partial x_i} \right) dR \tag{42a}$$

$$M_{IJ} = \sum_{e} \int_{R^e} N_I N_J \, dR \tag{42b}$$

$$F_I = \sum_{e} \int_{B_2^e} N_I Q \, dB \tag{42c}$$

Eq. (41) may be approximated by

$$[G] \left(\theta\{c\}_{t+\Delta t} + (1-\theta)\{c\}_t \right) + \frac{1}{\Delta t} [M] \left(\{c\}_{t+\Delta t} - \{c\}_t \right)$$

$$= \theta\{F\}_{t+\Delta t} + (1-\theta)\{F\}_t \tag{43}$$

where $\{c\}_t$ are known concentrations at time t; $\{c\}_{t+\Delta t}$ are unknown values of concentration at time $t+\Delta t$; θ is the time weighting factor $(0 \le \theta \le 1)$; and Δt is the time increment.

Eq. (43) may be rearranged, placing the unknown concentrations at the current time level on the left hand side, yielding

$$\theta [G]\{c\}_{t+\Delta t} + \frac{1}{\Delta t}[M]\{c\}_{t+\Delta t} = \frac{1}{\Delta t}[M]\{c\}_t + \theta\{F\}_{t+\Delta t} \tag{44}$$

$$+ (1-\theta)\{F\}_t - (1-\theta)[G]\{c\}_t$$

By setting θ equal to 0, 1, or 0.5, eq. (44) corresponds to the explicit method, the implicit method, or the Crank-Nicolson implicit time stepping scheme, respectively. The Crank-Nicolson scheme is second-order accurate but it requires slightly more computational effort than the implicit method and offers a higher order of accuracy in the calculated solution (Pinder and Gray, 1977, pp. 47-49).

2.3. Stream function-concentration (ψ-c) formulation

2.3.1. Governing equations

It is also possible to solve the given problem in terms of the stream function and concentration for a given flow domain. The governing equations relating the stream function with fluid velocity in two dimensions is defined as

$$v_1 = \frac{\partial \psi}{\partial x_2} \tag{45a}$$

$$v_2 = -\frac{\partial \psi}{\partial x_1} \tag{45b}$$

For an isotropic porous medium, eq. (10) may be substituted into eqs. (45a) and (41b) yielding

$$\frac{\partial \psi}{\partial x_2} = -K_o \frac{\mu_o}{\mu}\left[\frac{\partial h}{\partial x_1} + \varepsilon \frac{c}{c_1} e_1\right] \tag{46a}$$

$$\frac{\partial \psi}{\partial x_1} = K_o \frac{\mu_o}{\mu}\left[\frac{\partial h}{\partial x_2} + \varepsilon \frac{c}{c_1} e_2\right] \tag{46b}$$

If we assume that K_o, μ_o, and μ are independent of spatial coordinates, then the hydraulic head terms in eqs. (46a) and (46b) can be eliminated by cross differentiation as follows

$$\frac{\partial^2 \psi}{\partial x_2 \partial x_2} = -K_o \frac{\mu_o}{\mu}\left[\frac{\partial^2 h}{\partial x_2 \partial x_1} + \frac{\partial}{\partial x_2}\left(\varepsilon \frac{c}{c_1} e_1\right)\right] \tag{47a}$$

$$\frac{\partial^2 \psi}{\partial x_1 \partial x_1} = K_o \frac{\mu_o}{\mu}\left[\frac{\partial^2 h}{\partial x_1 \partial x_2} + \frac{\partial}{\partial x_1}\left(\varepsilon \frac{c}{c_1} e_2\right)\right] \tag{47b}$$

It should be noted that for the above assumption to be valid, the porous medium and fluid must be homogeneous. In addition μ_o/μ must be unity.

Adding eqs. (47a) and (47b) together, and noting that the e_1 term can be dropped if the x_2 coordinate is pointed in the vertical direction, yields

$$\frac{\partial}{\partial x_i} \left(\frac{\partial \psi}{\partial x_i} \right) = K_o \left[\frac{\partial}{\partial x_1} \left(\varepsilon \frac{c}{c_1} e_2 \right) \right] \tag{48}$$

Similarly, eqs. (45a) and (45b) may be substituted into eq. (12) to yield

$$\frac{\partial}{\partial x_i} \left(D \frac{\partial c}{\partial x_i} \right) = \left[\frac{\partial \psi}{\partial x_2} \frac{\partial c}{\partial x_1} - \frac{\partial \psi}{\partial x_1} \frac{\partial c}{\partial x_2} \right] + \frac{\partial c}{\partial t} \tag{49}$$

Eqs. (4), (48), and (49) form the required set of equations for the ψ-c finite element formulation.

2.3.2. Reduction of governing equations to dimensionless form

In addition to using eqs. (13), (14), and (15) to reduce the above required set of equations to dimensionless form, an additional equation is needed to describe the dimensionless stream function ψ^*, where

$$\psi^* = \frac{\psi}{Vd} \tag{50}$$

It is now possible to reduce eq. (48) to dimensionless form. Substituting eqs. (13) and (14) into eq. (48) yields

$$\frac{1}{d} \frac{\partial}{\partial x_i^*} \left(\frac{\partial \psi}{\partial x_i^*} \right) = \frac{K_o}{d} \varepsilon \, e_2 \frac{\partial c^*}{\partial x_i^*} \tag{51}$$

Substitution of eqs. (15) and (50) into eq. (51) yields

$$\frac{\partial}{\partial x_i^*} \left(\frac{\partial \psi}{\partial x_i^*} \right) = \frac{K_o}{V} \varepsilon \, e_2 \left(\frac{\partial c^*}{\partial x_i^*} \right) \tag{52}$$

Similarly, substitution of eqs. (13) and (14) into eq. (49) yields

$$\frac{1}{d^2} \frac{\partial}{\partial x_i^*} \left(D \frac{\partial c^*}{\partial x_i^*} \right) = \frac{1}{d^2} \left[\frac{\partial \psi}{\partial x_2^*} \frac{\partial c^*}{\partial x_1^*} - \frac{\partial \psi}{\partial x_1^*} \frac{\partial c}{\partial x_2^*} \right] + \frac{D_o}{d} \frac{\partial c^*}{\partial t^*} \tag{53}$$

Substituting eqs. (15) and (50) into eq. (53) and simplifying yields

$$\frac{\partial}{\partial x_i^*} \left(D^* \frac{\partial c^*}{\partial x_i^*} \right) = \frac{Vd}{D_o} \left[\frac{\partial \psi^*}{\partial x_2^*} \frac{\partial c^*}{\partial x_1^*} - \frac{\partial \psi^*}{\partial x_1^*} \frac{\partial c^*}{\partial x_2^*} \right] + d \frac{\partial c^*}{\partial t^*} \tag{54}$$

Eqs. (25), (52), and (54) form the required set of dimensionless equations for the ψ^*-c^* system.

2.3.3. ψ-c finite element formulation

The Galerkin approach will be applied to the dimensional ψ-c governing equations, i.e. eqs. (48) and (49). The Galerkin criterion requires that

$$\int_R N_I \left[\frac{\partial}{\partial x_i} \left(\frac{\partial \hat{\psi}}{\partial x_i} \right) - K_o \varepsilon \left(\frac{\partial}{\partial x_1} \left(\frac{\hat{c}}{c_1} e_2 \right) \right) \right] dR = 0 \tag{55}$$

and

$$\int_R N_I \left[\frac{\partial}{\partial x_i} \left(D \frac{\partial \hat{c}}{\partial x_i} \right) - \left(\frac{\partial \hat{\psi}}{\partial x_2} \frac{\partial \hat{c}}{\partial x_1} - \frac{\partial \hat{\psi}}{\partial x_1} \frac{\partial \hat{c}}{\partial x_2} \right) - \frac{\partial \hat{c}}{\partial t} \right] dR = 0 \tag{56}$$

where

$$\hat{\psi} = N_I(x_i) \psi_I(t) \tag{57a}$$

$$\hat{c} = N_I(x_i) c_I(t) \tag{57b}$$

Applying Green's theorem to the second order term in eq. (55) yields

$$\int_B N_I \frac{\partial \hat{\psi}}{\partial x_i} n_i \, dB - \int_R \frac{\partial N_I}{\partial x_i} \frac{\partial N_J}{\partial x_i} \psi_J \, dR - \int_R K_o \varepsilon \frac{e_2}{c_1} \frac{\partial \hat{c}}{\partial x_1} \, dR = 0 \qquad (58)$$

Incorporating the fluid flux boundary conditions,

$$\frac{\partial \hat{\psi}}{\partial x_2} = q \, n_1$$

$$\text{on } B_2 \qquad\qquad (59)$$

$$\frac{\partial \hat{\psi}}{\partial x_1} = -q \, n_2$$

where q is the outward normal fluid flux, eq. (58) becomes

$$\left[\int_R \frac{\partial N_I}{\partial x_i} \frac{\partial N_J}{\partial x_i} \, dR \right] \psi_J = \int_{B_2} N_I q (n_1 n_2 - n_2 n_1) \, dB - \int_R N_I K_o \frac{\varepsilon e_2}{c_1} \frac{\partial \hat{c}}{\partial x_1} \, dR$$

$$= - \int_R N_I K_o \, \varepsilon \frac{e_2}{c_1} \frac{\partial \tilde{c}}{\partial x_1} \, dR \qquad (60)$$

Since the fluid flux boundary condition term (B_2) vanishes, the remaining boundary condition states that $\hat{\psi}$ is prescribed on B_1.

Applying Green's theorem to the second order derivative term in eq. (56) yields

$$\int_B N_I D \frac{\partial \hat{c}}{\partial x_i} n_i \, dB - \left[\int_R D \frac{\partial N_I}{\partial x_i} \frac{\partial N_J}{\partial x_i} \, dR \right] c_J$$

$$- \left[\int_R N_I \left(\frac{\partial N_J}{\partial x_1} \frac{\partial \hat{\psi}}{\partial x_2} - \frac{\partial \hat{\psi}}{\partial x_1} \frac{\partial N_J}{\partial x_2} \right) dR \right] c_J - \int_R N_I N_J \frac{dc_J}{dt} \, dR = 0 \qquad (61)$$

Incorporating the concentration flux boundary condition on B_2' given in eq. (33), eq. (61) becomes

$$\left[\int_R \left(D \frac{\partial N_I}{\partial x_i} \frac{\partial N_J}{\partial x_i} + N_I \left(\frac{\partial N_J}{\partial x_1} \frac{\partial \hat{\psi}}{\partial x_2} - \frac{\partial \hat{\psi}}{\partial x_1} \frac{\partial N_J}{\partial x_2} \right) \right) dR \right] c_J$$

$$+ \int_R N_I N_J \frac{dc_J}{dt} \, dR = \int_{B_2'} N_I Q \, dB \qquad (62)$$

For steady state conditions, eq. (62) reduces to

$$\left[\int_R \left(D \frac{\partial N_I}{\partial x_i} \frac{\partial N_J}{\partial x_i} + N_I \left(\frac{\partial N_J}{\partial x_1} \frac{\partial \hat{\psi}}{\partial x_2} - \frac{\partial \hat{\psi}}{\partial x_1} \frac{\partial N_J}{\partial x_2} \right) \right) dR \right] c_J = \int_{B_2'} N_I Q \, dB \qquad (63)$$

2.3.4. Solution procedure

For steady state conditions, the uncoupled eqs. (60) and (63) can be written in matrix form as

$$[B]\{\psi\} = \{P\} \qquad (64a)$$

$$[E]\{c\} = \{S\} \qquad (64b)$$

where

$$B_{IJ} = \sum_e \int \frac{\partial N_I}{\partial x_i} \frac{\partial N_J}{\partial x_i} \, dR \qquad (65a)$$

$$P_I = \sum_e - \int_R N_I K_o \, \varepsilon \, \frac{e_2}{c_1} \frac{\partial \hat{c}}{\partial x_1} \, dR \tag{65b}$$

$$E_{IJ} = \sum_e \left[-\int_{R^e} \left(D \frac{\partial N_I}{\partial x_i} \frac{\partial N_J}{\partial x_i} + N_I \left(\frac{\partial N_J}{\partial x_1} \frac{\partial \hat{\psi}}{\partial x_2} - \frac{\partial \hat{\psi}}{\partial x_1} \frac{\partial N_J}{\partial x_2} \right) \right) dR \right] \tag{65c}$$

$$S_I = \sum_e \int_{B_2',e} N_I \, Q \, dB \tag{65d}$$

Solving eqs. (60) and (63) simultaneously results in the matrix equation

$$[M]\{\Omega\} = \{T\} \tag{66}$$

where

$$[M_{IJ}] = \begin{bmatrix} e_{IJ} & f_{IJ} \\ 0 & h_{IJ} \end{bmatrix} \tag{67a}$$

$$\{\Omega_J\} = \begin{Bmatrix} \psi_J \\ c_J \end{Bmatrix} ; \quad \{T_I\} = \begin{Bmatrix} T_{I1} \\ T_{I2} \end{Bmatrix} \tag{67b}$$

and

$$e_{IJ} = \sum_e \int_{R^e} \frac{\partial N_I}{\partial x_i} \frac{\partial N_J}{\partial x_i} \, dR \tag{68a}$$

$$f_{IJ} = \sum_e \int_{R^e} N_I K_o \varepsilon \, \frac{e_2}{c_1} \frac{\partial N_J}{\partial x_1} \, dR \tag{68b}$$

$$h_{IJ} = \sum_e \int_{R^e} \left(D \frac{\partial N_I}{\partial x_i} \frac{\partial N_J}{\partial x_i} + N_I \left(\frac{\partial N_J}{\partial x_1} \frac{\partial \hat{\psi}}{\partial x_2} - \frac{\partial \hat{\psi}}{\partial x_1} \frac{\partial N_J}{\partial x_2} \right) \right) dR \tag{68c}$$

$$T_{I1} = 0 \tag{68d}$$

$$T_{I2} = \sum_e \int_{B_2^! e} N_I \, Q \, dB \tag{68e}$$

For the simultaneous solution, the coefficient matrix [M] is formed by guessing the initial value of $\hat{\psi}$. Iteration is performed until satisfactory convergence is achieved.

3. Computer Code Implementation

The preceding finite element formulation has been incorporated into computer code CLFEM5 (Appendix I). This code incorporates the upstream weighted residual approach (Huyakorn and Nilkuha, 1978), which due to its generality, can make use of either the Galerkin basis functions (i.e. N_I) or asymmetric weighting functions (i.e. W_I). By using asymmetric weighting functions, numerical oscillation associated with high Peclet numbers can be diminished, as will be demonstrated in the sea water intrusion calibration problem.

The discretization data used as input data in CLFEM5 (i.e. number of nodes and their locations, nodal connections, element numbering, etc.) can either be generated tediously by hand or automatically by using either of the codes, MGENET or MESHG. By supplying only a minimal amount of information, MGENET can generate regular grids (i.e. rectangular elements) with or without grading. For irregular grid configurations, MESHG can be used to obtain discretization data such as that used to generate the mesh for the two-dimensonal flow domain in Fig. 18. It is also possible to generate simple, regular, rectangular meshes using the built in mesh generator in CLFEM5.

Once the discretization data has been obtained, aquifer parameters and boundary conditions are supplied, along with the discretization data, as input data for CLFEM5. For problems involving steady flow, the nodal hydraulic head values are obtained independently of the concentration values by solving the flow equation first. These hydraulic head values are then used as input data which are used to calculate nodal velocities needed in the transport equation to obtain the nodal concentration values.

Once the nodal hydraulic head and concentration values have been calculated. the output data can be read directly into plotting routines TPLOT1, TPLT1G, HCPLTC, or HCPLTG to generate plots of discretization data; hydraulic head or concentration contours; nodal velocity vectors; and distribution of nodal hydraulic head or concentration values along the top and bottom nodal boundaries (for regular meshes only such as as in the sea water intrusion problem).

A schematic of the order of implementation for these programs is given in Fig. 3.

```
        ┌─────────────────────┐
        │  MESHG or MGENET     │
        │                      │
        │  (Mesh Generator)    │
        └─────────────────────┘
                   │
                   ▼
    ┌─────────────────────────────────────────┐
    │             CLFEM5                        │
    │                                           │
    │ (Hydraulic head and concentration solver) │
    └─────────────────────────────────────────┘
         ↙                        ↘
┌─────────────────────────┐   ┌─────────────────────────────┐
│        TPLOT1           │   │        HCPLTC               │
│          or             │   │          or                 │
│        TPLT1G           │   │        HCPLTG               │
│                         │   │                             │
│ (Mesh, contours, and gradient│ (Hydraulic head (or concentra-│
│ plotting routine in either   │ tion) vs. horizontal distance │
│ COMPLOT or TECTRONIX format) │ plotting routine in either    │
│                         │   │ COMPLOT or TECTRONIX format;  │
│                         │   │ used for regular meshes)      │
└─────────────────────────┘   └─────────────────────────────┘
```
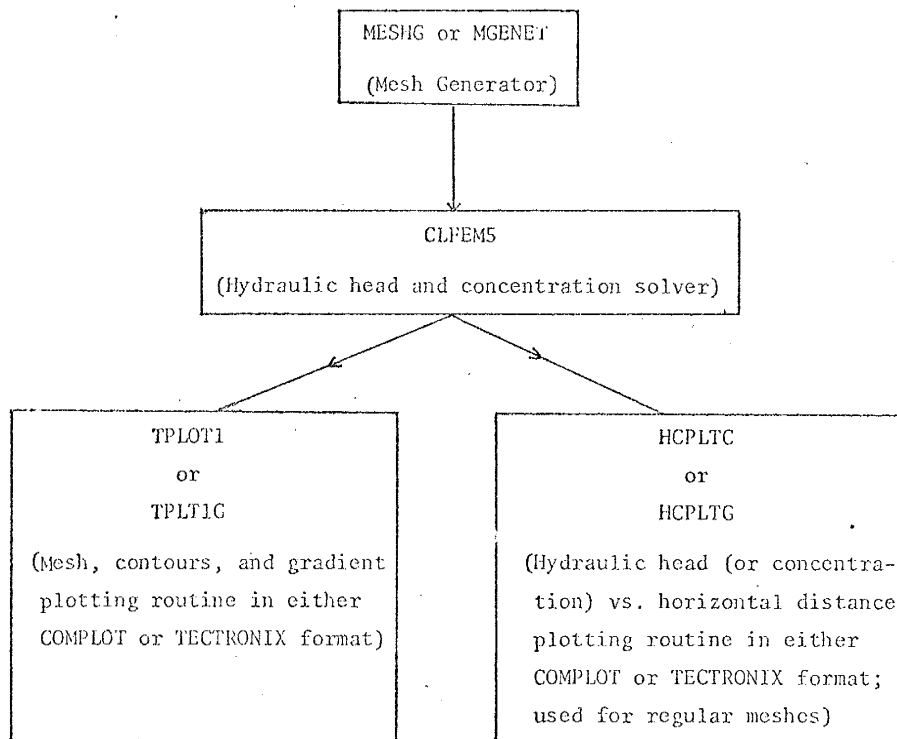
Fig. 3 Order of implementation for the computer codes used to obtain discretization data, hydraulic head and concentration nodal values, and plots.

4. Application of Computer Code to the Problem of Sea Water Intrusion

In order to check the performance of computer code CLFEM5, a test problem identical to the sea water intrusion problem (Fig. 4(a)) of Huyakorn and Taylor (1977) has been run and a comparison of these results appears in Table 2. The relatively minor differences in results are due in part to the use of 4 node quadrilateral elements versus 8 node quadrilateral elements, although both methods use the Galerkin finite element approach.

From the boundary conditions depicted in Fig. 4(a), it is assumed that the normalized sea water concentration occurs at the sea boundary and that the flow is horizontal there. A more accurate set of boundary conditions would be based on the pressure and mass flux conditions at the sea boundary. It should be noted that the boundary conditions in Fig. 4(a) are only approximate. A more complete discussion of the appropriate boundary conditions may be found in Bear (1972, pp.622-624).

Plots of the element numbering scheme used, hydraulic head contours, and velocity distribution appear in Figs. 5(a), (b), and (c). Fig. 6 shows the calculated hydraulic head distribution along the top and bottom nodal boundaries.

Since this problem involves moderately convective-dominated transport, due to a Peclet number of 10, numerical oscillation is observed in the normalized concentration values at the top boundary obtained using the Galerkin approach as seen in Fig. 7. In order to damp out this oscillation, the upstream weighting finite element technique described by Huyakorn and Taylor (1977) was applied and the effect of its application is shown in Fig. 8. The normalized concen-

$U/(K_o \epsilon) = 0.263$; $Pe = Ud/D_o = 10$; $L/d = 2$

$\frac{\partial h}{\partial x_1} = \frac{-1}{150}$

$v_1 = 1$

$v_2 = 0$

$c = 0$

$h = \rho_s - \epsilon x_2$

$K_o = 150$

$c = 1$; $D_o = 0.1$

$\epsilon = 0.025$; $U = 1$

(a)

$U/(K_o \epsilon) = 0.263$; $Pe = Ud/D_o = 10$; $L/d = 2$

$\frac{\partial h}{\partial x_1} = \frac{-1}{19.2}$

$v_1 = 1$

$v_2 = 0$

$c = 0$

$h = \rho_s - \epsilon x_2$

$K_o = 19.2$

$c = 1$; $\epsilon = 0.198$

$D_o = 0.1$; $U = 1$

(b)
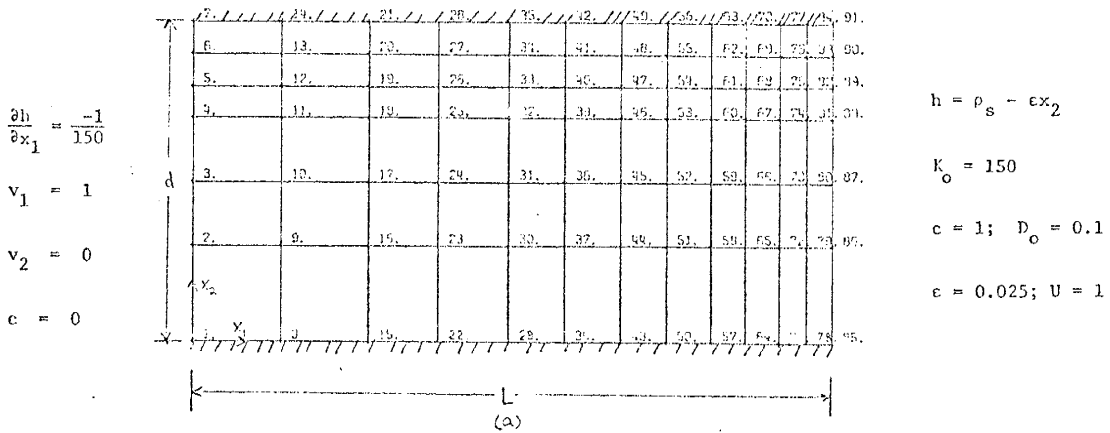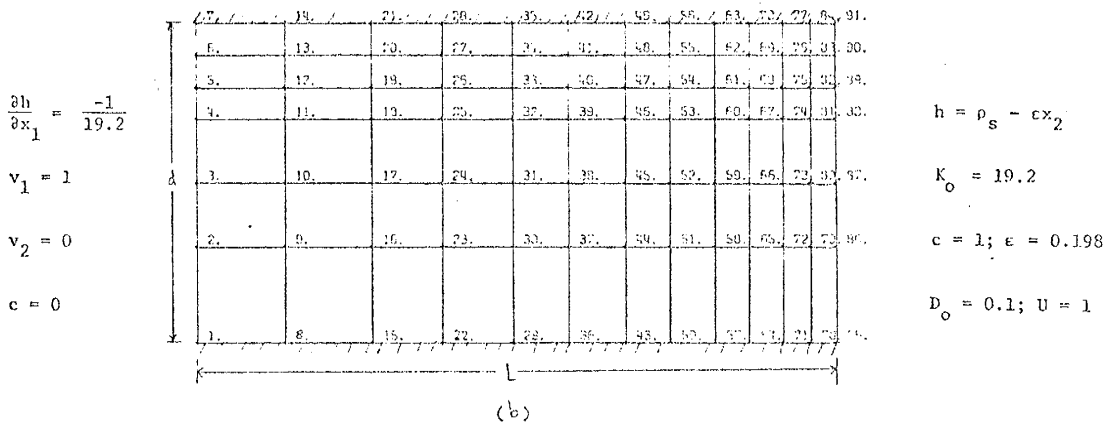
Fig. 4 Node numbering scheme and boundary conditions for the sea water intrusion problem involving (a) unsaturated salt water and (b) saturated salt water (after Huyakorn and Taylor, 1977, p. 1.142). The above conditions are compatible for use with the h-c model.

(a)

6	12	18	24	30	36	42	48	54	60	66	72
5	11	17	23	29	35	41	47	53	59	65	71
4	10	16	22	28	34	40	46	52	58	64	70
3	9	15	21	27	33	39	45	51	57	63	69
2	8	14	20	26	32	38	44	50	56	62	68
1	7	13	19	25	31	37	43	49	55	61	67

(b)

Hydraulic Head
Contour Value

$3 = 1.02305$

$2 = 1.01658$

$1 = 1.01010$

$0 = 1.00363$

(c)

Magnitude of Dimensionless Velocity: 0 ——— 10
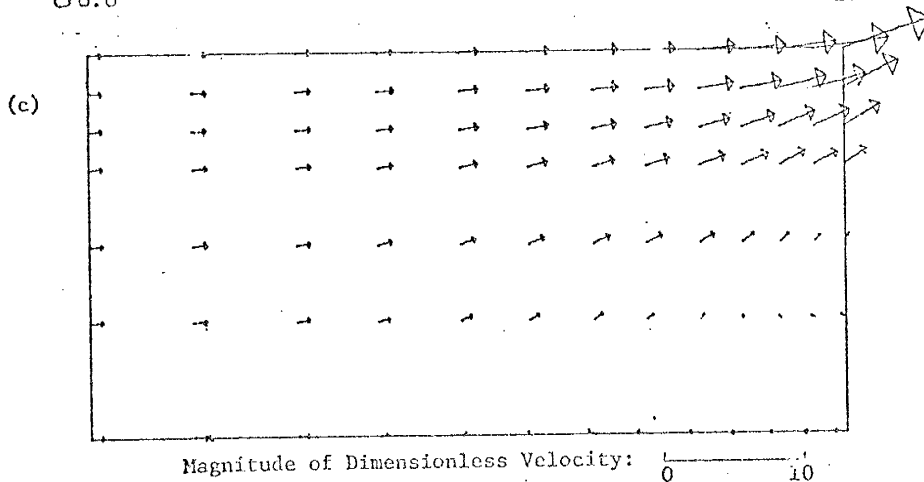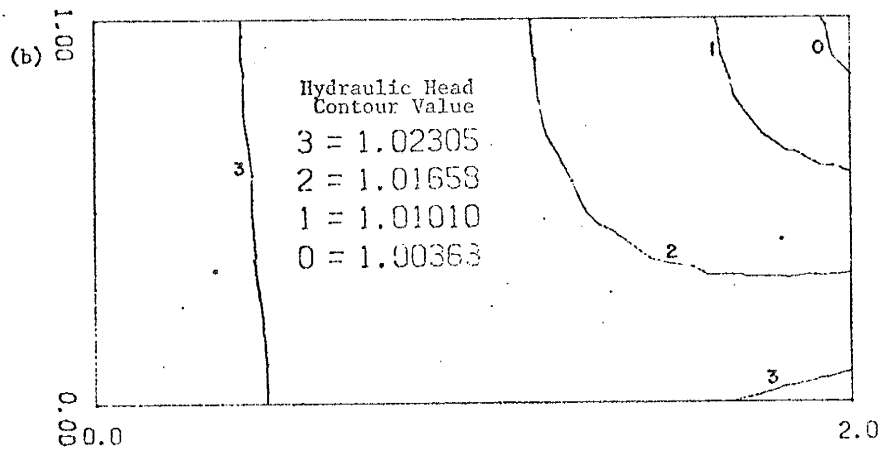
Fig. 5   (a) Element numbering scheme used for the sea water intrusion problem; (b) hydraulic head contours and (c) related velocity distribution obtained for the sea water intrusion problem, Pe = 10.

Node Number	Horizontal Distance	Galerkin (without viscosity effect)	Galerkin (with viscosity effect)	Galerkin (Huyakorn and Taylor, 1977)	Galerkin (saturated with viscosity effects)	Asymmetric weighting func.
Top Nodes						
7	0.000	0.00000	0.00000	0.0000	0.00000	0.00000
14	0.275	-0.00000	-0.00000	-0.0000	-0.00000	0.00045
21	0.55	0.00002	0.00001	0.0003	0.00003	0.00167
28	0.77	0.00015	0.00017	0.0001	0.00002	0.00410
35	0.99	0.00115	0.00111	0.0021	0.00138	0.00857
42	1.166	0.00298	0.00303	0.0043	0.00350	0.01522
49	1.342	0.00883	0.00786	0.0182	0.00995	0.02512
56	1.483	0.01187	0.01255	0.0096	0.01355	0.03819
63	1.624	0.03858	0.02982	0.0661	0.04133	0.05723
70	1.730	-0.01016	-0.00658	0.0167	-0.00604	0.08564
77	1.833	0.22650	0.16021	0.3590	0.22823	0.14691
84	1.920	-0.41127	-0.37912	-0.1772	-0.37527	0.31138
91	2.000	1.00000	1.00000	1.0000	1.00000	1.00000
Bottom Nodes						
1	0.000	0.00000	0.00000	0.0000	0.00000	0.00000
8	0.275	-0.00001	-0.00000	-0.0005	-0.00008	0.00107
15	0.55	0.00008	0.00001	0.0044	0.00023	0.00549
22	0.77	0.00802	0.00475	0.0135	0.01207	0.01968
29	0.99	0.07363	0.06985	0.0848	0.09327	0.06947
36	1.166	0.21958	0.22724	0.2363	0.25671	0.18669
43	1.342	0.44243	0.47015	0.4593	0.48841	0.42807
50	1.483	0.63648	0.66369	0.6358	0.67895	0.65026
57	1.624	0.80155	0.81851	0.7805	0.85541	0.83131
64	1.730	0.89402	0.90103	0.8700	0.91515	0.90863
71	1.833	0.95543	0.95675	0.9368	0.96651	0.96572
78	1.920	0.98615	0.98592	0.9748	0.99035	0.99059
85	2.000	1.00000	1.00000	1.0000	1.00000	1.00000

Table 2   Comparison of normalized salt concentration values for top and bottom boundaries for the sea water intrusion problem, Pe = 10 (Huyakorn and Taylor, 1977).
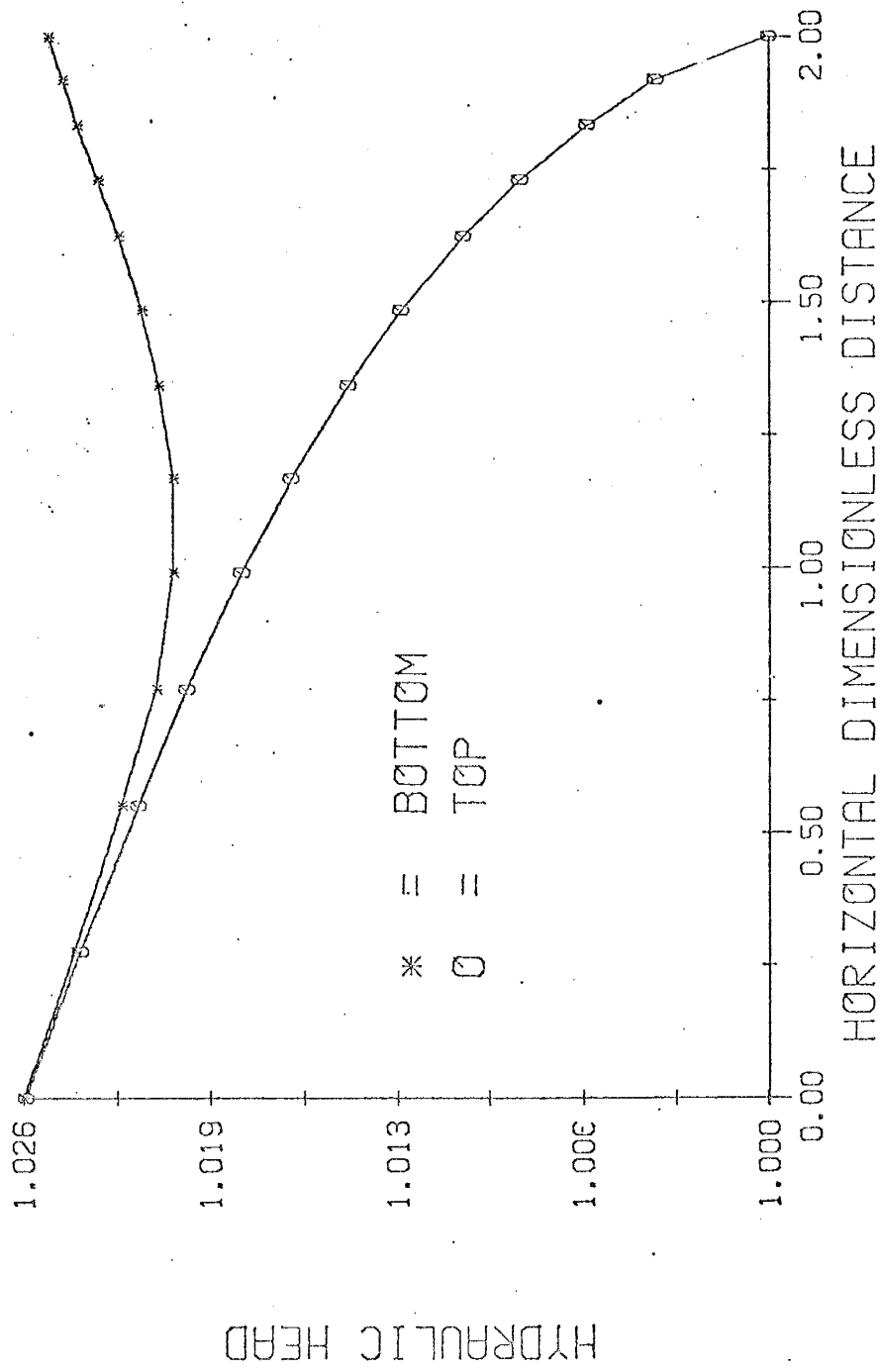
Fig. 6   Hydraulic head distribution along the top and bottom nodal
boundaries for the sea water intrusion problem, Pe = 10.
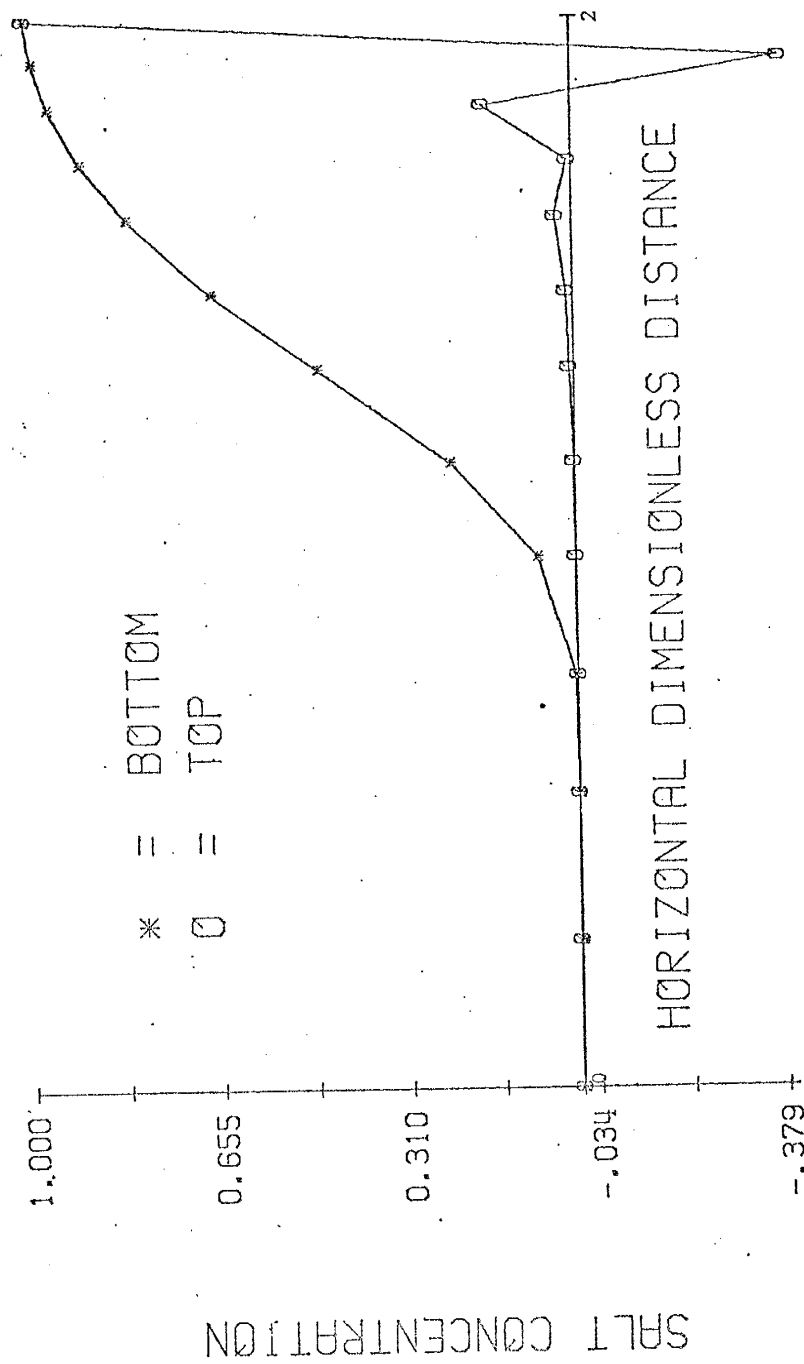
Fig. 7 Plot of concentration versus distance obtained for the sea water intrusion problem, Pe = 10, using the Galerkin approach for top and bottom nodal boundaries.
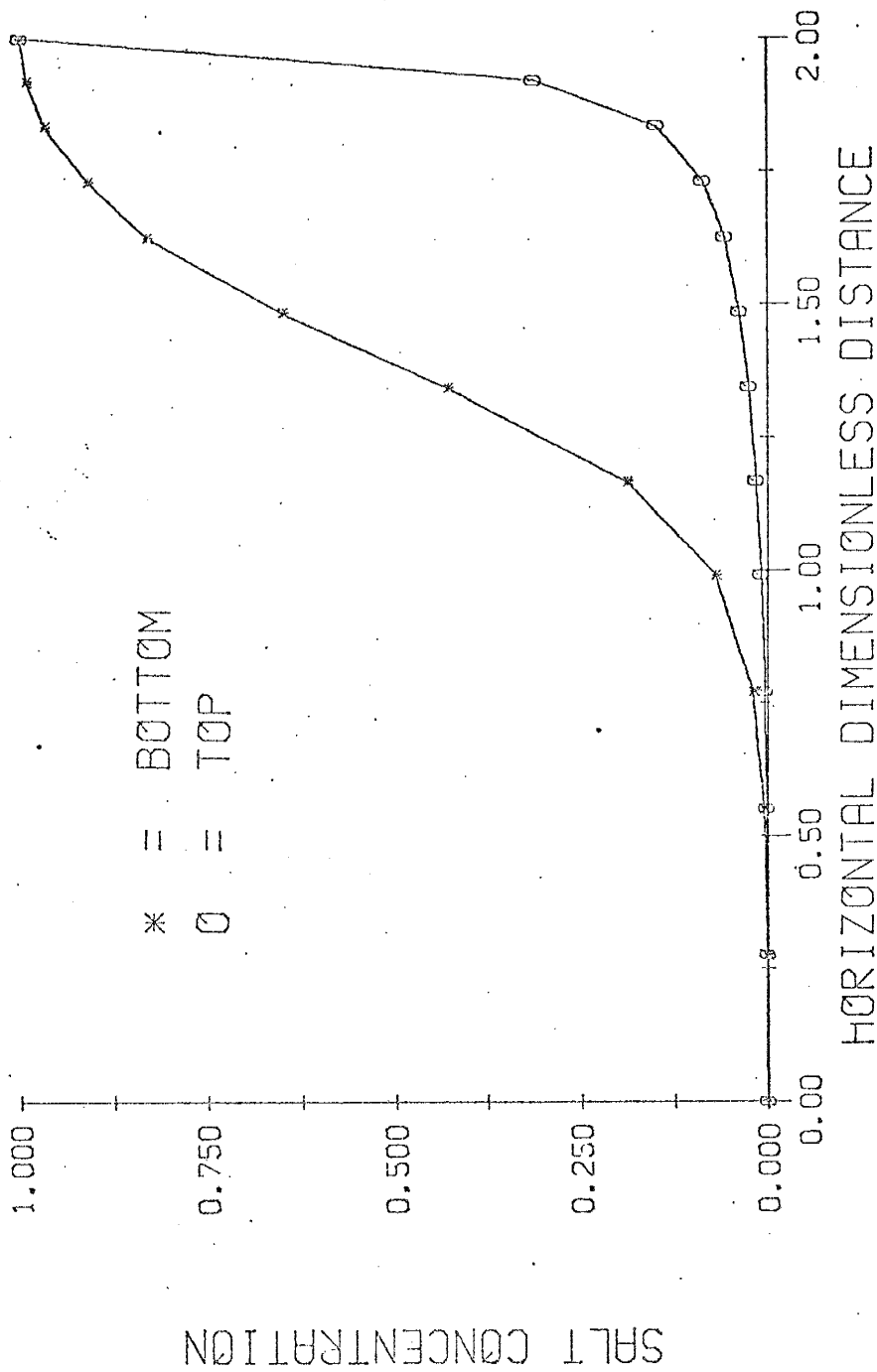
Fig. 8 Plot of salt concentration versus horizontal dimensionless
distance obtained for the sea water intrusion problem,
Pe = 10, using asymmetric weighting functions, for top and
bottom nodal boundaries.

tration contours obtained using the Galerkin and upstream weighting finite element techniques appear in Figs. 9(a) and (b). A numerical solution obtained using the correct boundary conditions would be much better as the approximate boundary conditions produce the unrealistic vertical concentration contours near the upper part of the outflow boundary.

Since this problem is in essence a test of CLFEM5, and since CLFEM5 was modified to take into account the effect of viscosity changes, a comparison can be made of the importance of this modification before and after its introduction by running the problem of Fig. 4(a) twice. The results of these two runs appear in Table 2 under the headings "Galerkin without viscosity effect" and "Galerkin with viscosity effect". A visual comparison reveals little difference between the values in these two columns, hence at low concentrations viscosity effects do not play an important role.

In order to test the importance of viscosity in a situation of saturated concentration, such as in a halite "aquifer", the problem in Fig. 4(a) was modified to simulate the intrusion of a saturated NaCl solution into a fresh water aquifer. The conditions for this problem appear in Fig. 4(b). The concentration values for this run when viscosity was taken into consideration appear in Table 2 and differ only slightly from the unsaturated-run values. This indicates that viscosity effects are not significant in the problem of sea water intrusion, regardless of the degree of saturation.

One of the first field calibrations of a finite element model related to the problem of contaminant transport was done by Pinder (1973) in his analysis of ground water contamination on Long Island, New York,

(a)

```
Concentration Contour Value
    3  =  1.000
    2  =  0.690
    1  =  0.345
```

1.00

0.00 0.0

(a)

2.0

(b)

```
Concentration Contour Value
    3  =  1.000
    2  =  0.750
    1  =  0.500
    0  =  0.250
```

1.00

0.00 0.0

(b)

2.0
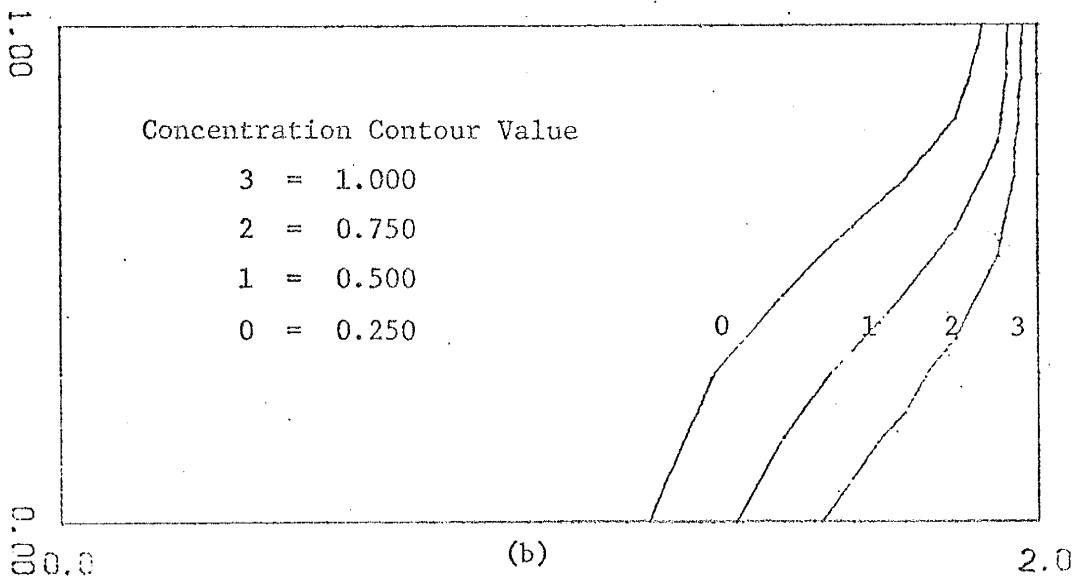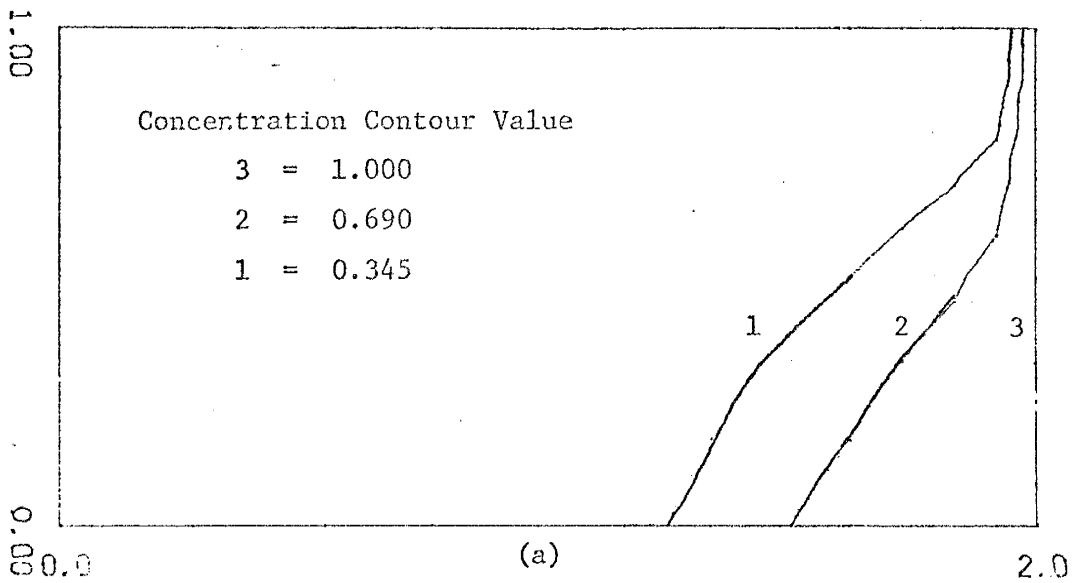
Fig. 9   Contours of normalized concentration for the sea water
intrusion problem, Pe = 10, using (a) the Galerkin
approach and (b) asymmetric weighting functions.

5. Contaminant Transport in the Los Medanos Area, Eddy and Lea Counties, New Mexico

5.1. Introduction

The salt deposits of the Los Medanos area, Eddy and Lea Counties, New Mexico, have been studied since 1972 as a possible geologic unit for a waste-isolation repository pilot plant. Bedded salt has the desirable repository properties of hydrologic and geologic stability, plasticity, and favorable thermal characteristics (Mercer and Orr, 1977, p.9).

5.2. Hydrogeology

Previous investigations of the hydrogeology of the Los Medanos area have been made by Mercer and Orr(1977) and Lambert and Mercer (1977). Los Medano: is part of a gently sloping terrain that rises eastward from the Pecos River to the "caprock" of the Llano Estacado (Fig. 10). Topographic relief is generally less than 50 feet, and most geologic formations are covered with smoothly rounded hills of dune sand. Vegetation consists of mesquite, scrub oak, and other plants found in the northern Chihuahuan Desert. The annual precipitation averages 12 to 13 inches (Mercer and Orr, 1977, p.9).

The Los Medanos area is drained by the Pecos River, a perennial stream with headwaters in north-central New Mexico. Most local tributaries originate in the Guadalupe Mountains. The Pecos drainage system trends southeast through the western margin of the study area. The drainage east of the Pecos, which includes the Los Medanos area, is very poorly developed (Mercer and Orr, 1977, p.9).

The main topographic features in the vicinity of the Los Medanos
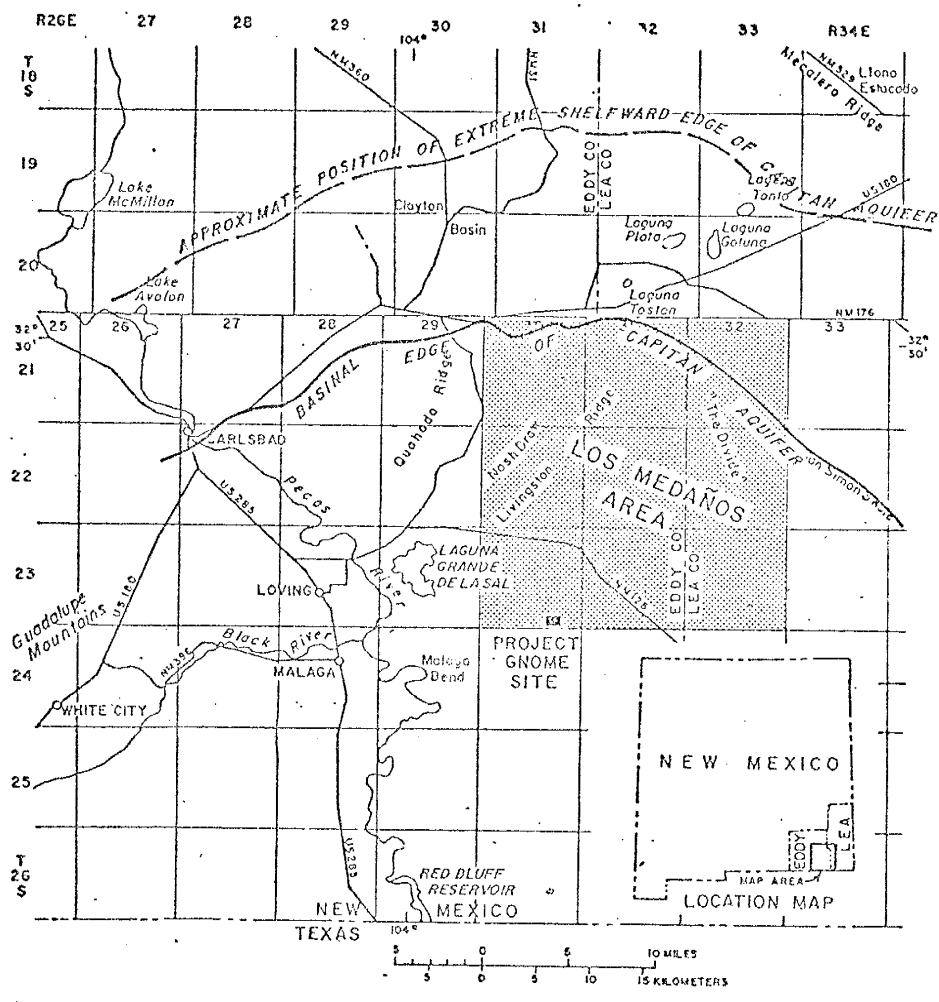
Fig. 10 Location map of Los Medanos area and vicinity (Mercer and Orr, 1977, p. 10).

area include the Guadalupe Mountains on the west; the Pecos River valley; the High Plains (Llano Estacado) and Mescalero Ridge to the east; and the pediment and alluvial plains that slope eastward from the Guadalupe Mountains and westward from the High Plains to the Pecos River (Fig. 10). The study area is mostly on pediment and alluvial plains east of the Pecos River. Erosional surface features have been modified extensively by solution, subsidence, and collapse. Locally, streams have exposed caliche and other rocks, but most of the area is mantled by dune sands. Some surface water drains eastward into closed depressions, but most of the precipitation is captured by sand dunes (Mercer and Orr, 1977, p.11).

Laguna Grande de la Sal, a large salt lake in Nash Draw east of Loving, contains water most of the year. Numerous small lakes (lagunas and playas) contain water only after heavy rains. Small tailings ponds have been extablished in closed depressions as a result of potash mining. Lake McMillan and Lake Avalon north of Carlsbad, and Red Bluff Reservoir on the Texas-New Mexico state line, are the only large water bodies in the region (Mercer and Orr, 1977, p.11).

The dominant solution depressions near Los Medanos area are Clayton Basin to the northwest, Nash Draw, which extends southward through the west-central part of the area, and San Simon Swale, which lies on the eastern margin (Fig.10). These features strongly affect the regional hydrology (Mercer and Orr, 1977, p.11).

5.3. Regional setting

Late Permian limestones of the Capitan reef deliniate the margins of the Delaware Basin where thick salt beds occur. The subsurface

geology of the Delaware Basin includes rocks ranging from Precambrian
to Quaternary in age. Precambrian crystalline basement rocks at depths
up to 19,500 feet are overlain by approximately 14,000 feet of pre-
evaporite Paleozoic rocks. Four thousand feet of Delaware Basin evapo-
rites overlie these sedimentary rocks. Permian, Triassic, and Quaternary
rock units are summarized in Table 3 (Mercer and Orr, 1977, p.11).

The basin evaporites (Ochoan Series) were accumulated during
Late Permian time (Table 3). They include the Castile, Salado, and
Rustler Formations. A thin red siltstone unit, the Dewey Lake Red Beds,
overlies the evaporite sequence. East of Nash Draw along Livingstone
Ridge, Triassic sandstone of the Santa Rosa Formation unconformably
overlies the Dewey Lake Red Beds. Holocene caliche of the Mescalero
surface and Holocene dune sand cap this Permian-Triassic stratigraphic
sequence throughout much of Los Medanos area (Fig.11). The Pleistocene
Gatuna Formation occurs as bolson-type deposits filling channels and
steep-walled valleys (Fig.12) (Mercer and Orr, 1977, p.11).

5.3.1. Rustler Formation

Of particular interest in this study is the Rustler Formation.
The Rustler contains anhydrite, gypsum, red beds, dolomite, limestone,
and halite. The thickness of the Rustler generally ranges from 200 feet
in the western part of the Delaware Basin to 600 feet in the eastern
part (Mercer and Orr, 1977, p.22). Two dolomite beds are recognized in
the Rustler and range between 20 and 30 feet thick (Fig.13). The upper
dolomite member (Magenta) is a finely crystalline, dense dolomite. The
lower dolomite member (Culebra) is vuggy, and is commonly associated
with some anhydrite. The Culebra member transmits water to wells at

DEPARTMENT OF THE INTERIOR
U.S. GEOLOGICAL
SURVEY

EXPLANATION

Ogallala Formation — TERTIARY

Triassic rocks, undivided — TRIASSIC

Dewey Lake Red Beds

Rustler Formation

Salado Formation — PERMIAN

Castile Formation

Capitan Limestone and Artesia Group, undivided
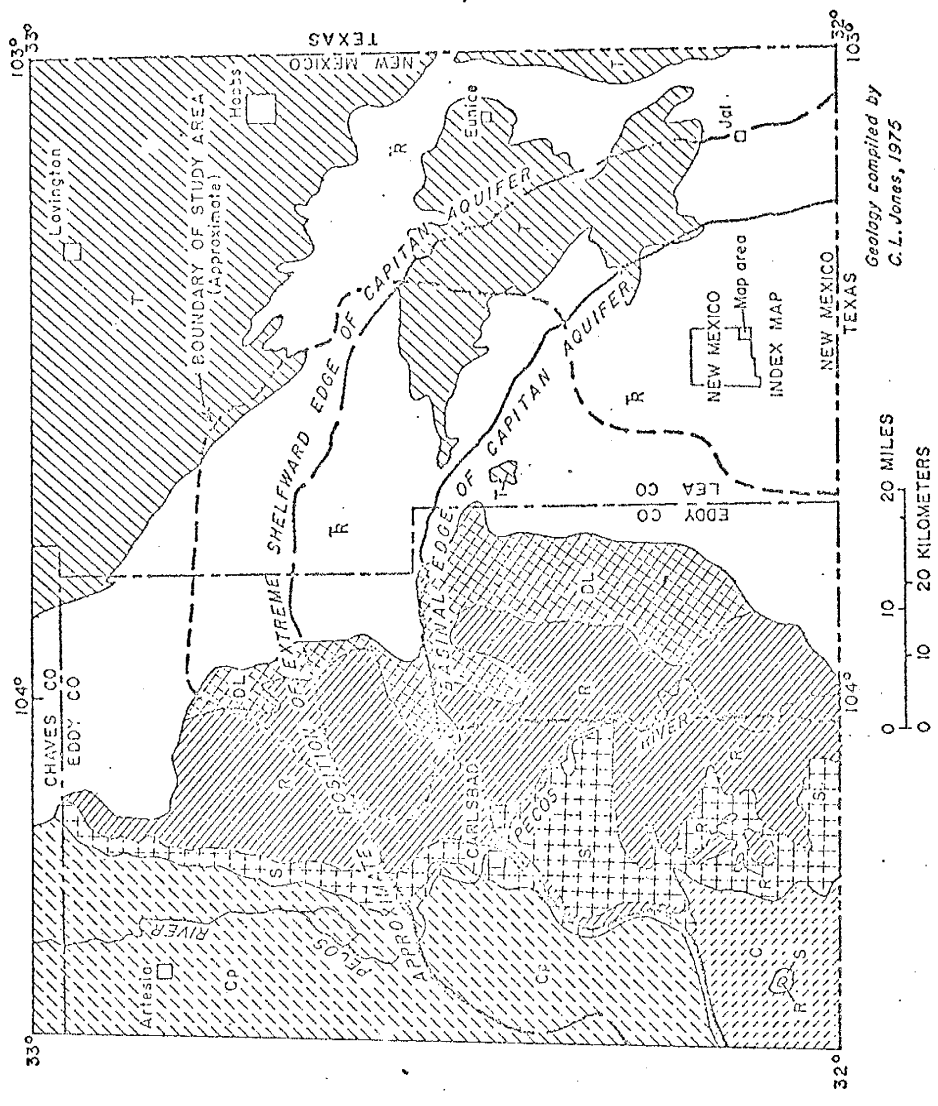
Fig. 11 Geologic map of Los Medanos area and vicinity (Mercer and Orr, 1977, p. 13).

Age			Rock Unit	Thickness (feet)	Description
Quaternary	Holocene		Sand of Mescalero surface	0-15	Dune sand, uniformly fine-grained, light-brown to reddish-brown
			— — — — — — — — — — UNCONFORMITY — — — — — — — — — —		
			Alluvium	0-300	Sand, silt, and conglomerate
			Caliche	0-5	Limestone, chalky, includes fragments of underlying rock
			— — — — — — — — — — UNCONFORMITY — — — — — — — — — —		
	Pleistocene(?)		Gatuna Formation	0-375	Sandstone and siltstone, poorly indurated, dominantly reddish-orange
			— — — — — — — — — — UNCONFORMITY — — — — — — — — — —		
Tertiary	Miocene		Ogallala Formation	25-175	Sandstone, fine- to medium-grained, tan, pink, and gray, locally conglomerate, and typically has resistant cap of well-indurated caliche
			— — — — — — — — — — UNCONFORMITY — — — — — — — — — —		
Triassic	Late Triassic		Chinle Formation	0-800	Mudstone shaly, reddish-brown and greenish-gray, interbedded lenses of conglomerate, and gray and reddish-brown sandstone
			Santa Rosa Sandstone	140-300	Sandstone, medium- to coarse-grained, commonly cross-stratified, gray and yellowish-brown, contains conglomerate and reddish-brown mudstone
			— — — — — — — — — — UNCONFORMITY — — — — — — — — — —		
Permian	Ochoan		Dewey Lake Red Beds	200-600	Siltstone and sandstone, very fine to fine-grained, reddish-orange to reddish-brown, contains interbedded reddish-brown claystone, small-scale laminati and cross-stratification common
			— — — — — — — — — — UNCONFORMITY — — — — — — — — — —		
			Rustler Formation	200-600	Anhydrite and rock salt with subordinate dolomite, sandstone, claystone, and polyhalite.
			Salado Formation	1,450-2,073	Rock salt with subordinate anhydrite, polyhalite, potassium ores, sandstone, and magnesite
			Castile Formation	1,300-2,000	Anhydrite and rock salt with subordinate limestone
	Guadalupian	Delaware Mountain Group	Capitan Limestone	1,600±	Limestone, massive, with dolomitized reef breccia
			Bell Canyon Formation	1,000±	Sandstone, brown and gray, with minor limestone and shale
			Cherry Canyon Formation	1,000±	Sandstone, gray and brown, with limestone and minor shale
			Brushy Canyon Formation	1,000±	Sandstone, gray, with brown and black shale and brown limestone

Table 3   Summary of rock units of Permian (Ochoan and Guadalupian) and younger age, Los Medanos area, Eddy and Lea Counties, New Mexico (Mercer and Orr, 1977, p. 12).
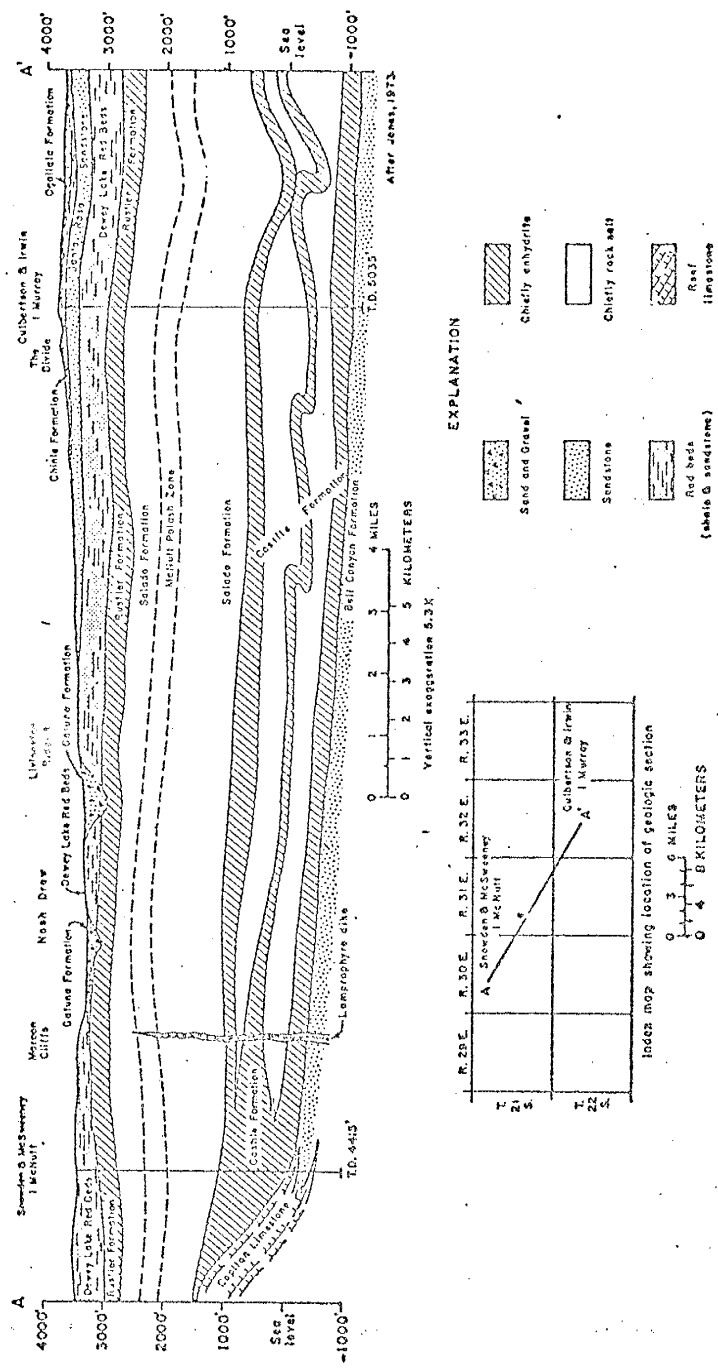
Fig. 12 Generalized geologic section of Los Medanos area (Mercer and Orr, 1977, p. 14).
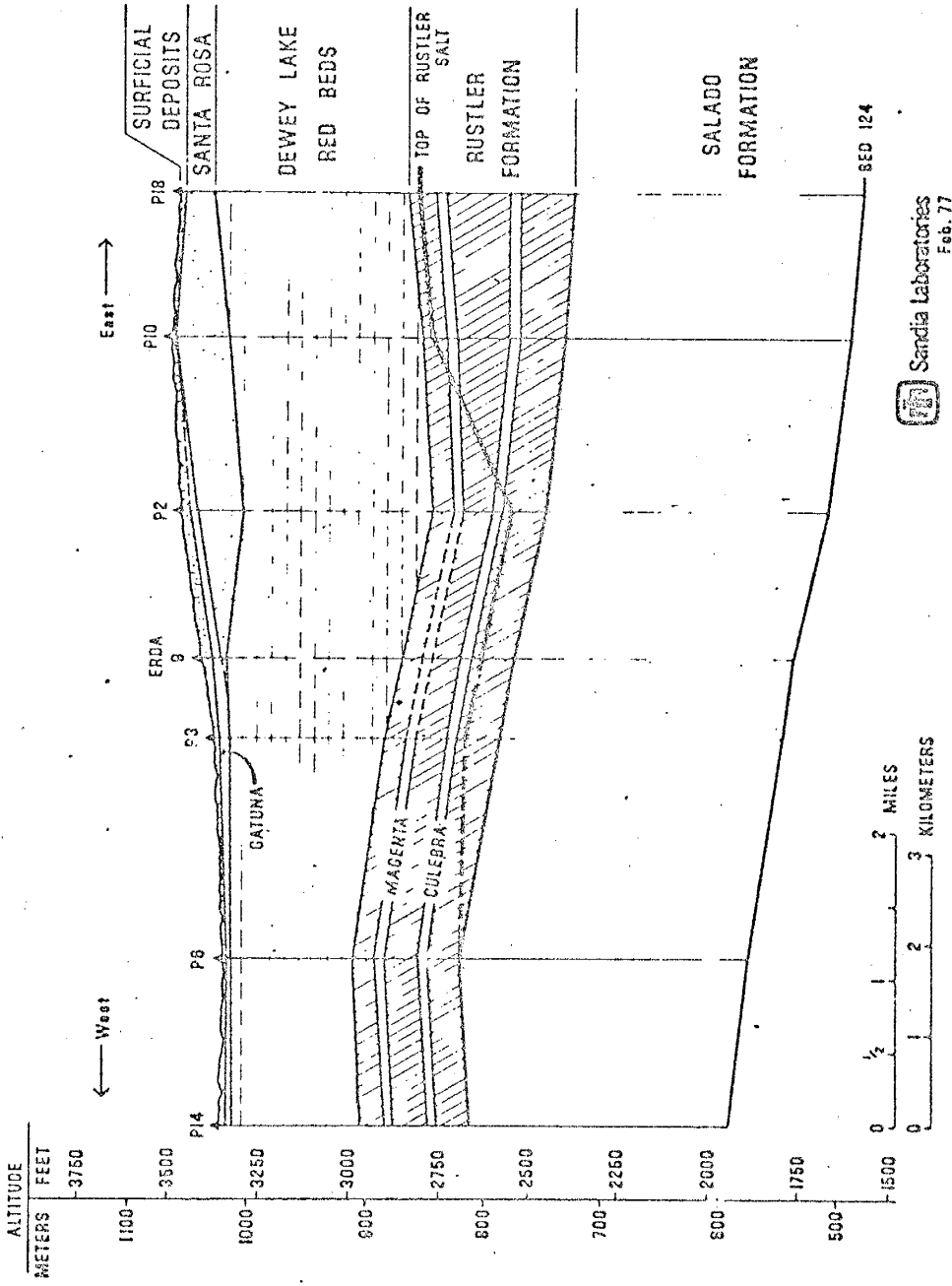
Fig. 13   Geologic section through the Los Medanos area (Lambert and Mercer, 1977, p.I-15).

a rate up to a few hundred gallons per minute south and west of the study area and is considered a major aquifer in these areas. The Magenta transmits only minor amounts of water and is not considered an important aquifer. Culebra water contains between 7,000 and 30,000 ppm dissolved solids, and the Magenta between 4,000 and 7,000 ppm. (Lambert and Mercer, 1977, p.I-2). Ground water from the Rustler discharges into the Pecos River at Malaga Bend, the principal direction of flow being toward the southwest.

5.4. Transport scenario simulated

The following transport scenario is strictly hypothetical and is not intended to be a definitive answer to a real problem. It is designed simply to test the effectiveness of the numerical model to address a potential situation.

A potential location for the proposed nuclear waste repository is within the salt beds of the Salado Formation. Ground water could potentially enter the repository from the Delaware Mountain Group through artesian flow. The hypothetical mechanism envisioned for the establishment of hydraulic communication between the Rustler, Salado, and Delaware Mountain Group might be through the inadvertent drilling of an uncased exploration borehole. Such an event, it is assumed, could cause water to flow up the borehole from the Delaware Mt. Group, become saturated with nuclear-waste contaminant, and enter the Rustler Formation from the borehole. The flow mechanisms within the Rustler could then disperse the contaminated water as a time related process.

5.5 Hydrologic parameters used and solution procedure

The numerical model presented in this thesis has been applied to the above contaminant transport scenario. It was assumed that the hydraulic head distribution could be approximated by the distribution shown in Fig. 14. Two zones of hydraulic conductivity within the Rustler Formation were assumed and their distribution and values appear in Fig. 15. The hydraulic conductivity in Zone 2 (Fig. 15) was assumed to be four times as great as that in Zone 1. The porosity of the Rustler was assumed to be 0.25 and the flow rate through the borehole entering the Rustler was set at 300 ft^3/day or 109,500 ft^3/year. Instead of using actual concentration levels, normalized concentrations were used by setting the saturated concentration level equal to unity at the borehole. This concentration was assumed to be constant with respect to time. Instead of dealing with a complex of radioactive materials, the contaminant was conservatively assumed to be salt, which simplified the problem by not having to deal with radioactive decay chains.

Although the total thickness of the Rustler Formation varies between 200 and 600 feet, the effective hydraulic thickness based on the thickness of the Magenta and Culebra aquifer members (Fig. 13) was set equal to 50 feet. When comparing this thickness with the overall area (1296 sq. miles), it is possible to neglect vertical flow components, hence the problem reduces to one of two-dimensional transport.

5.5.1. <u>One-dimensional transport</u>

As a preliminary analysis, a one-dimensional transport problem was solved along the line joining Los Medanos and Malaga Bend, shown
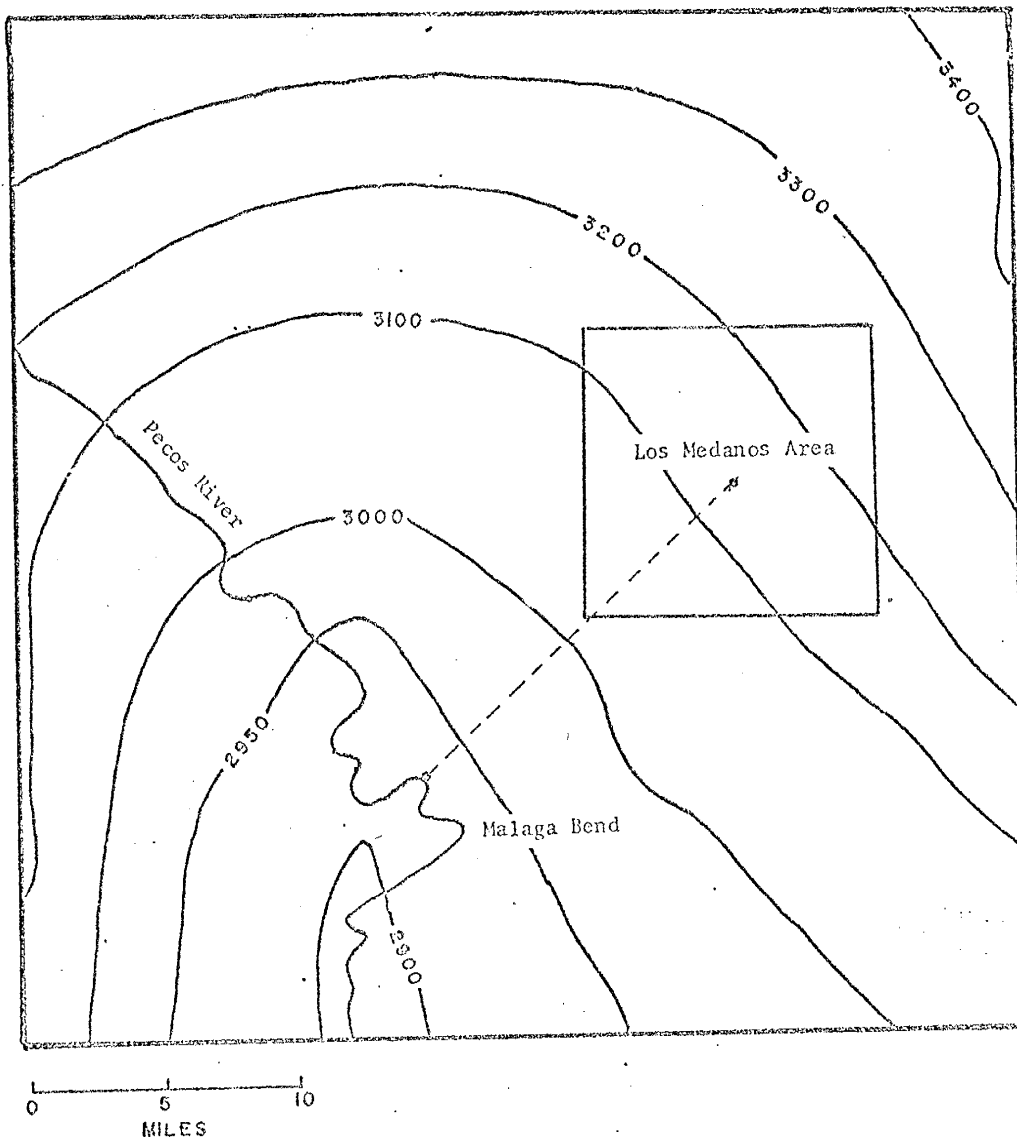
Fig. 14 Potentiometric map showing the hypothetical hydraulic head distribution within the Rustler Formation used to obtain the hydraulic head boundary conditions for the one- and two-dimensional contaminant transport problems.

Zone 1
$K_1 = 365$ ft/yr

Zone 2
$K_2 = 1460$ ft/yr

Pecos River

Hypothetical boundary

Los Medanos

Malaga Bend

Finite element boundary $\longrightarrow$

0   5   10
MILES

Fig. 15 Map showing the hypothethetical hydraulic conductivity boundary
        between zones 1 and 2, and the finite element adaption
        of the boundary to fit the finite element mesh of figure 18.

in Fig. 15. This 94,000 feet long line was equally divided into 40

equally sized elements. In order to give each element a reasonable

length to width ratio nearer to unity, the problem was artificially

transformed into a two-dimensional problem by giving each element a

"height" of 1000 feet. Hydraulic head boundary conditions were identi-

cally specified for the top and bottom nodes at locations of 0 feet,

14,100 feet, and 94,000 feet away from Los Medanos using the undisturbed

potentials of 3,150 feet, 3,083 feet, and 2,930 feet respectively. The

hydraulic conductivity values shown in Fig. 15 were divided at 14,100

feet away from Los Medanos. The problem was run for two different

values of dispersivity in Zone 2 (300 and 1200 feet), while the disper-

sivity in Zone 1 was kept constant at 300 feet. Each problem was run

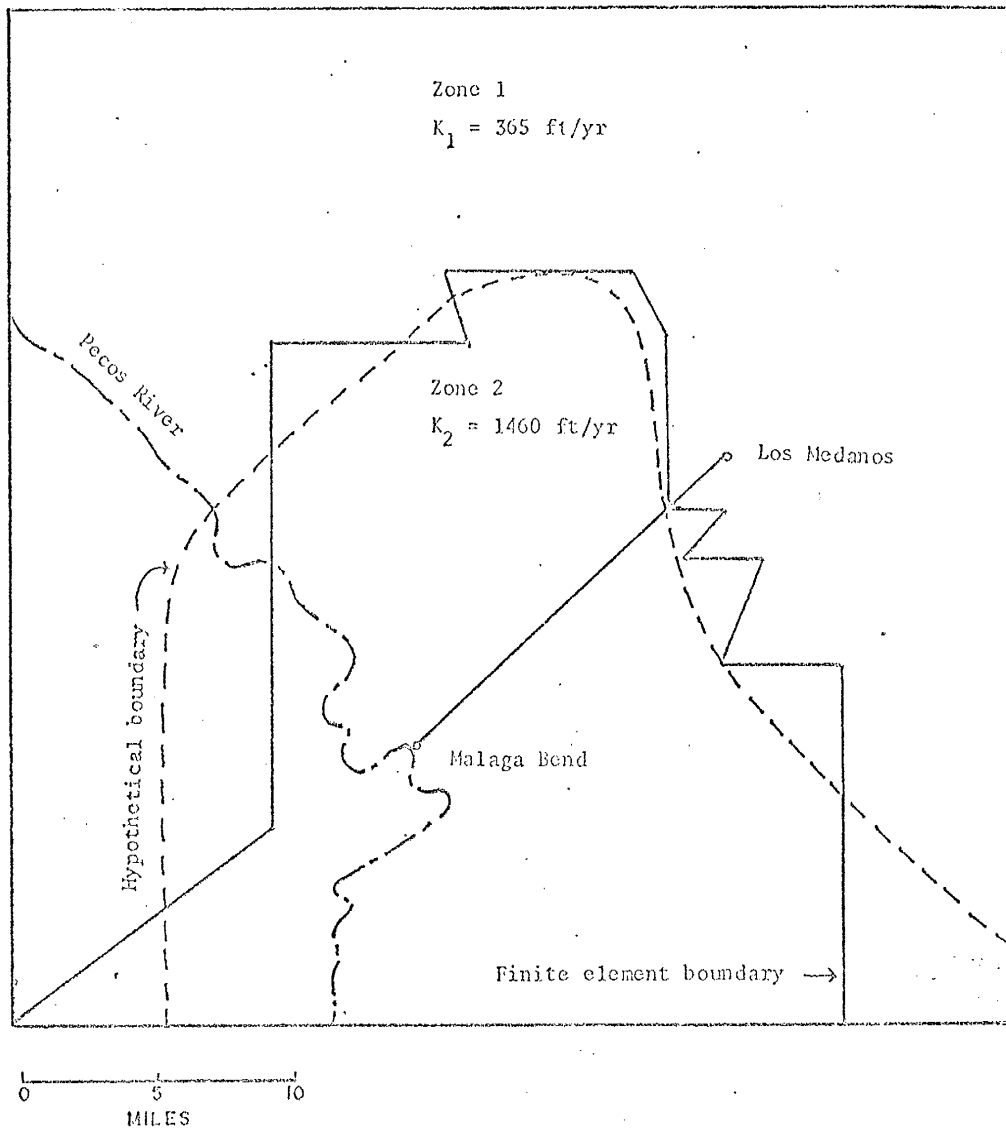for 40 time steps, each step of length 250 years. The results of

these runs appear in Figs. 16 and 17.

The results in Figs. 16 (a) and 16 (b) reveal similar results for

the two different values of dispersivity used. The higher value, how-

ever, causes the concentration front to be more highly smeared or

flattened. The analytical solution is represented by the sharp front

designated by dashed lines for the various times indicated. The dashed

lines pass through the center of mass of the approximate solutions

at times of 2,500 years and 6,000 years. Fig. 17 indicates that at a

dispersivity of 300 feet, the breakthrough concentration at Malaga

Bend reaches the saturated concentration more quickly than for the

dispersivity value of 1,200 feet--i.e. the 300 feet value causes less

dispersion, and therefore less dilution, of the contaminant at times

later than 8,500 years. One-dimensional flow is the most conservative

analysis of the contaminant transport process since dispersion and
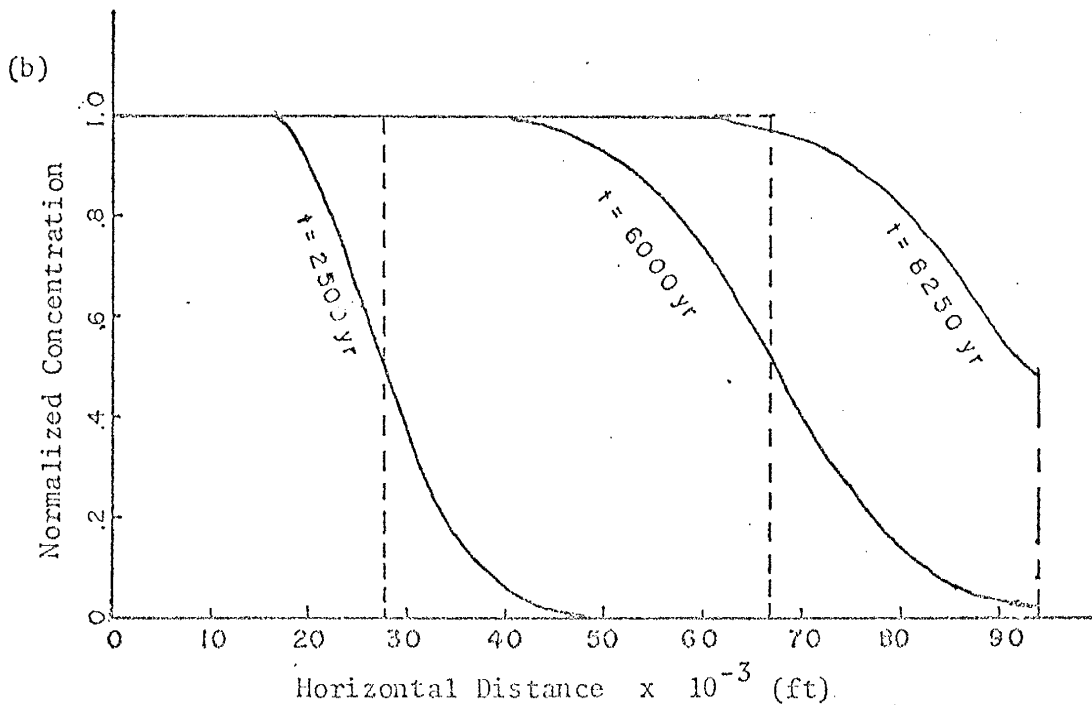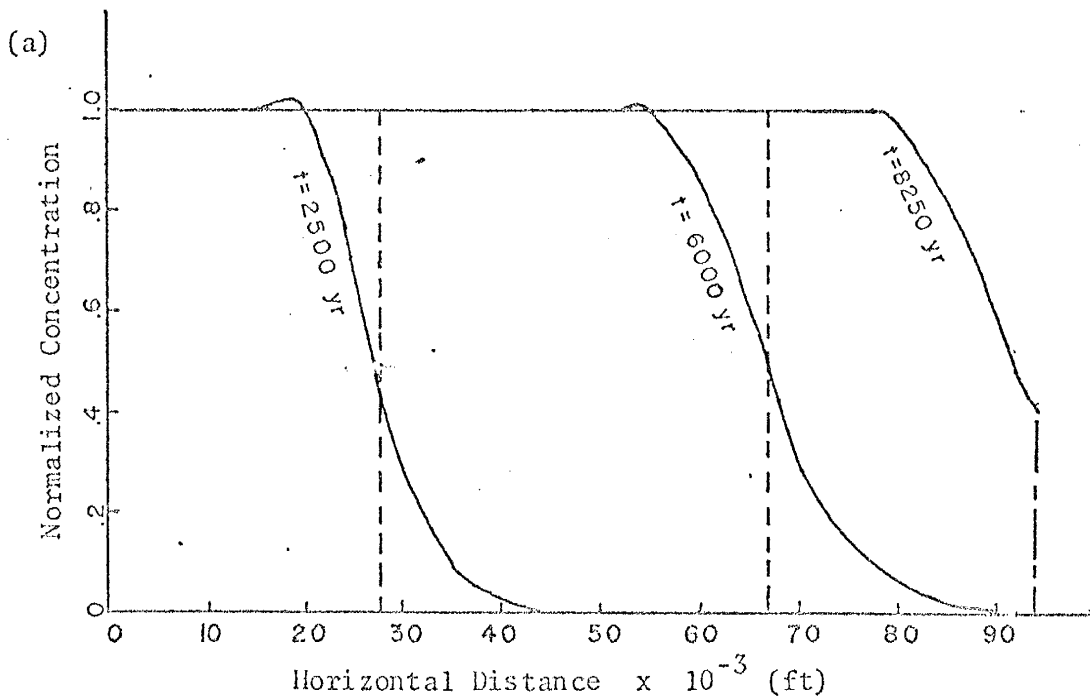
Fig. 16 Plots of normalized concentration versus horizontal distance at times of 2500, 6000, and 8250 years for the one-dimesional contaminant transport problem where (a) the dispersivity in Zone 2 (α_2) equals 300 feet and (b) α_2 equals 1200 feet.
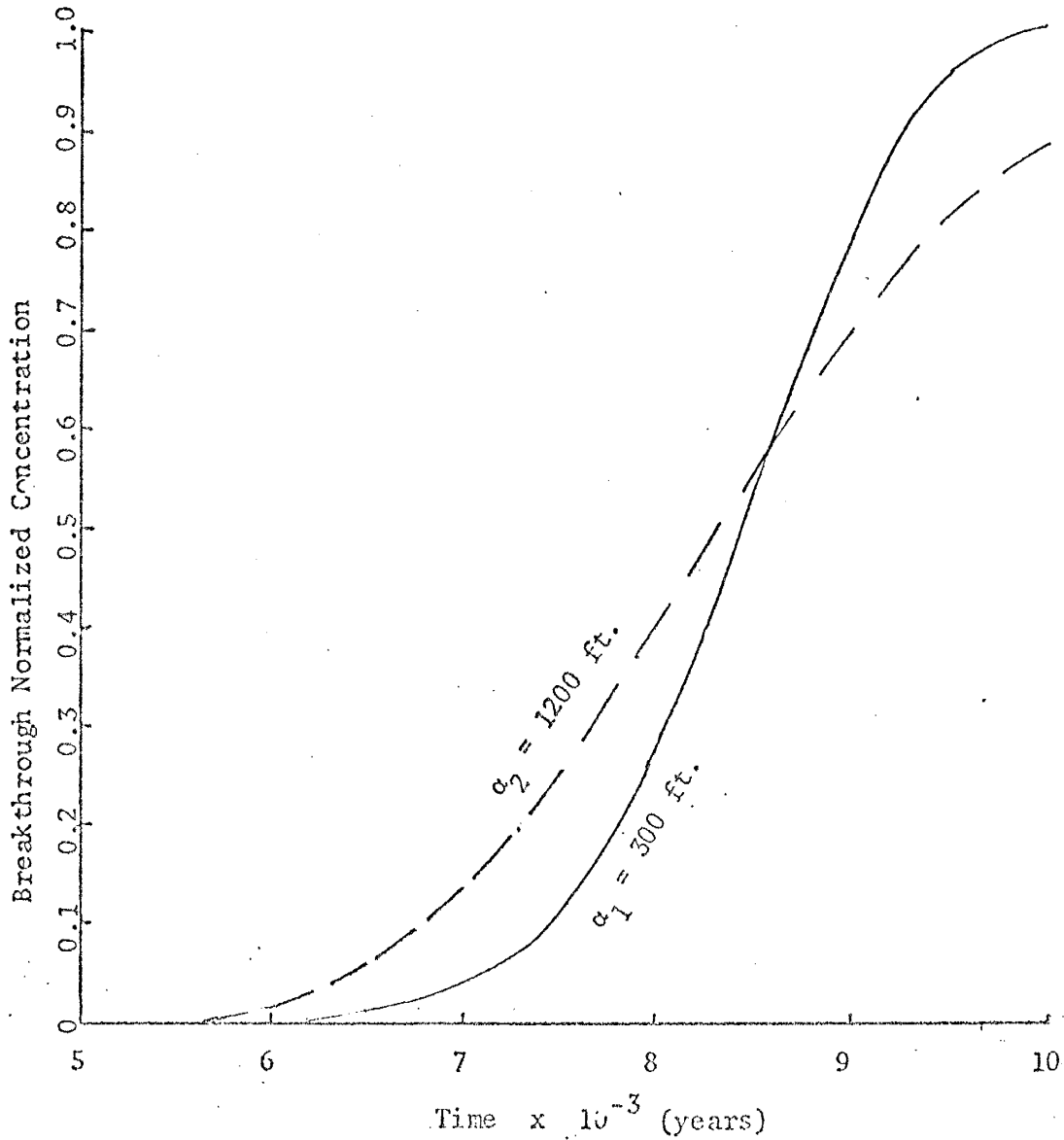
Fig. 17 Plot of normalized breakthrough concentrations versus time
for the one-dimensional contaminant transport problems where
Zone 1 dispersivities (α_1) are kept equal to 300 feet, and
Zone 2 dispersivities (α_2) are set at 300 and 1200 feet
respectively.

convection are restricted to one dimension. A less conservative but more realistic analysis will be shown for the case of two-dimensional contaminant transport.

5.5.2. Two-dimensional transport using irregular mesh

The preceeding problem was run for the two-dimensional case using the irregular mesh depicted in Figs. 18 and 19. The undisturbed hydraulic head values and associated velocity values shown in Figs. 20 and 21 were obtained independently of the concentration values by specifying the boundary hydraulic head values, obtained by interpolation of the values of Fig. 14, and solving for steady-state hydraulic head values. These hydraulic head values were then used to solve for the nodal, normalized, concentration values shown in Figs. 23 through 29.

Numerical oscillation was observed when dispersivities of 2,400 feet and lower were used (Fig. 23). The plot of normalized concentration versus horizontal distance at t = 32,000 years in Fig. 23(b) not only shows negative concentration values but also a violation of the boundary condition, $\partial c/\partial x = 0$, at node 16. As an attempt to damp out these problems, upstream weighting was applied, although unsuccessfully, and the results appear in Fig. 24. From Fig. 23 it is seen that that an acceptible numerical solution can only be obtained by using an exces- sively high dispersivity value (i.e. 24,000 feet). It should be emphasized that the dispersivity value of 24,000 feet is quite unrealistic from a physical standpoint.

Concentration contours at various times using dispersivities of 300 and 24,000 feet appear in Figs. 25 through 29. As expected, the
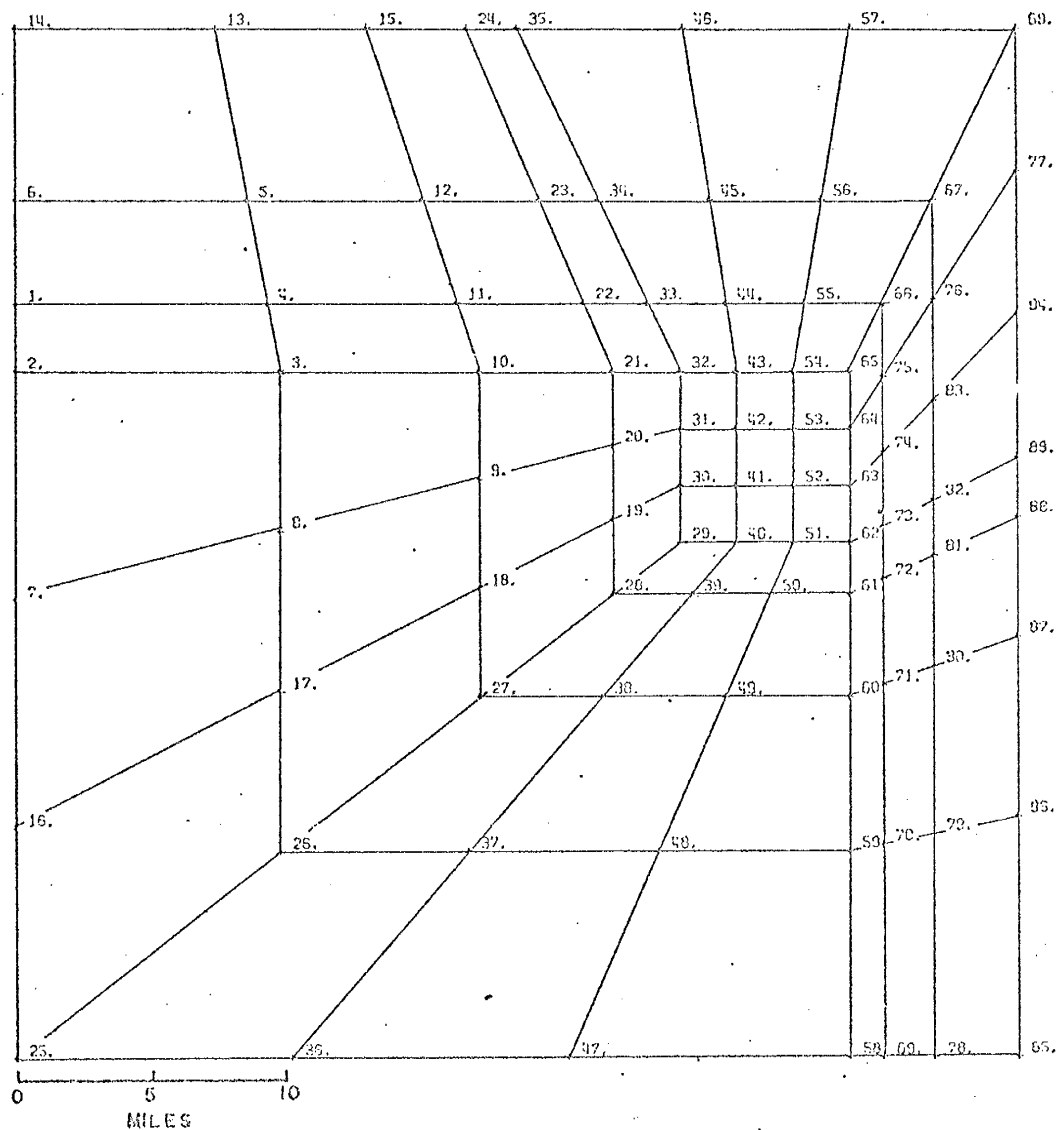
Fig. 18 Finite element mesh and optimized nodal numbering scheme generated
by computer code MESHG for the two-dimensional flow problem.
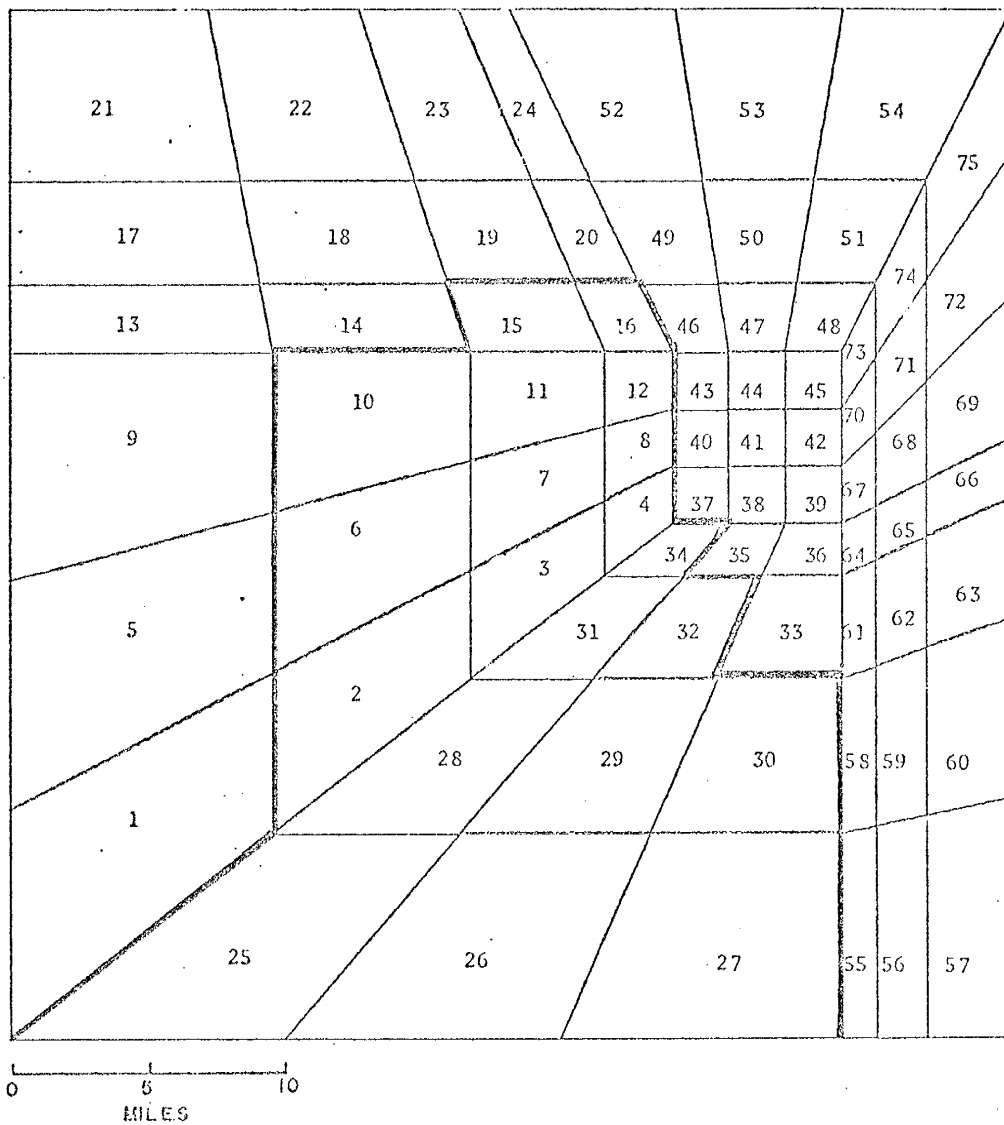
Fig. 19   Finite element mesh and element numbering scheme generated by computer
          code MESHG for the two-dimensional flow problem showing the division of
          two zones with varying hydraulic conductivities (indicated by heavy line.)
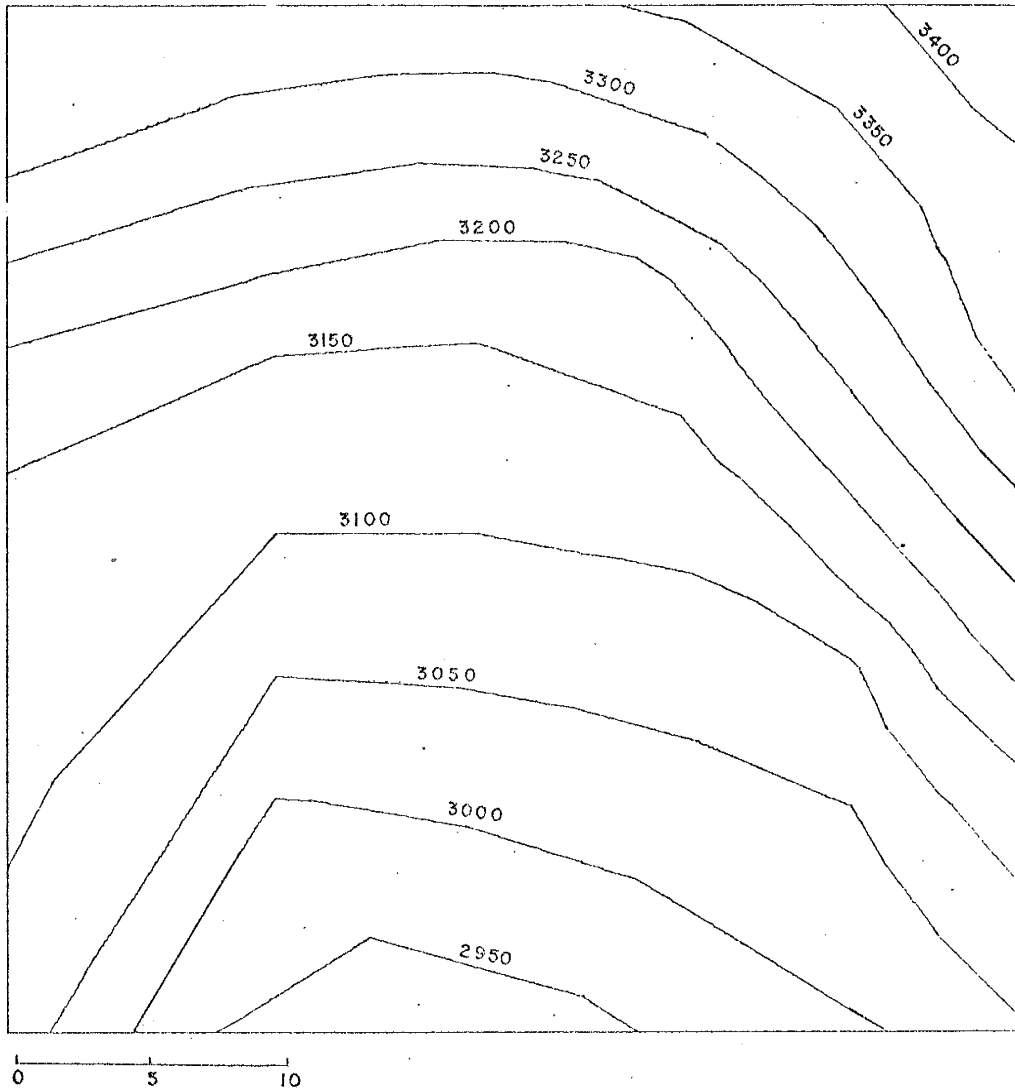
Fig. 20   Hydraulic head distribution obtained using the mesh in
Fig. 18   and specifying only the boundary hydraulic head
values obtained through interpolation from Fig. 14
using undisturbed hydraulic potentials. Values are in feet.
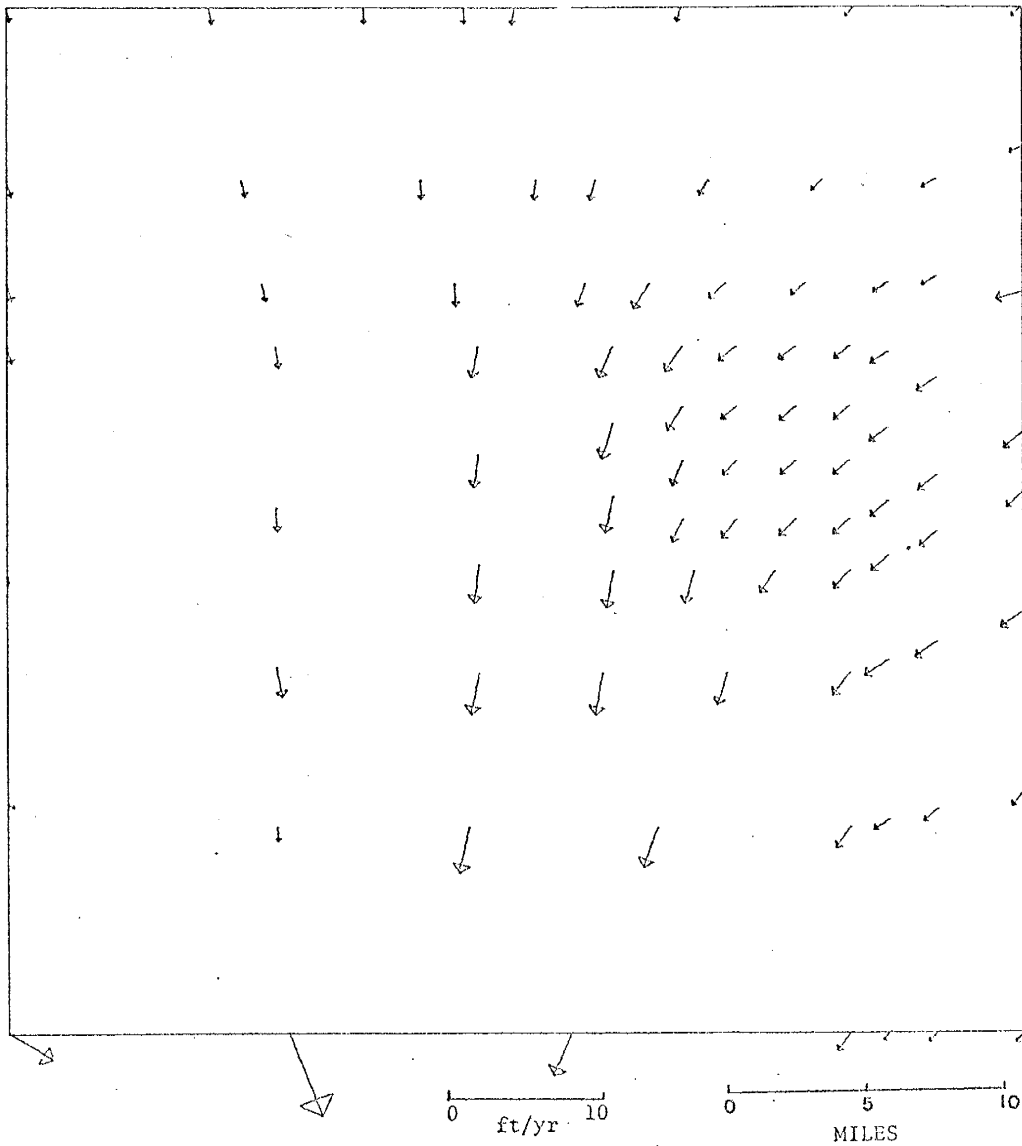
Fig. 21 Velocity distribution obtained from the irregular mesh
in Fig. 18 associated with undisturbed hydraulic potentials.

dispersivity value of 24,000 feet causes the concentration plume to move more quickly than for the value of 300 feet.

The dimensionless parameters affecting the occurence of numerical oscillation are the Peclet number (Pe = d/α, where d is the characteristic length of the elements used and α is the dispersivity); and the Courant number (Cr = $V\Delta t/\Delta x$, where V is the characteristic velocity; Δt is the time increment; and Δx is the length of the element). To minimize the occurence of numerical oscillation, the Peclet number should be below 10 and the Courant number less than or equal to 1. The large elements along the left and bottom boundaries of Fig. 18 produce unacceptible Peclet numbers and a poor approximation of the boundary condition, $\partial c/\partial x = 0$.

In order to overcome these difficulties, it is possible to design a new mesh consisting of uniform rectangular elements with a smaller characteristic length. This has been done and the results appear in the following section.

Figs. 25 and 26 show the calculated normalized concentration contours for times of 4,000 and 16,000 years at a dispersivity of 300 feet. In order to fascilitate contouring, negative concentration values obtained were set equal to zero. Numerical oscillation at t = 32,000 years was so extreme as to make contouring impossible. The concentration contour of 0.05 does not reach Malaga Bend after 16,000 years (Fig. 26) although the principle direction of flow should be along a line drawn from Los Medanos to Malaga Bend (Fig.14). By overlaying the velocity distribution of Fig. 21 over Fig. 14 it can be seen that this flow direction has been distorted, probably due to the selection of the mesh used.
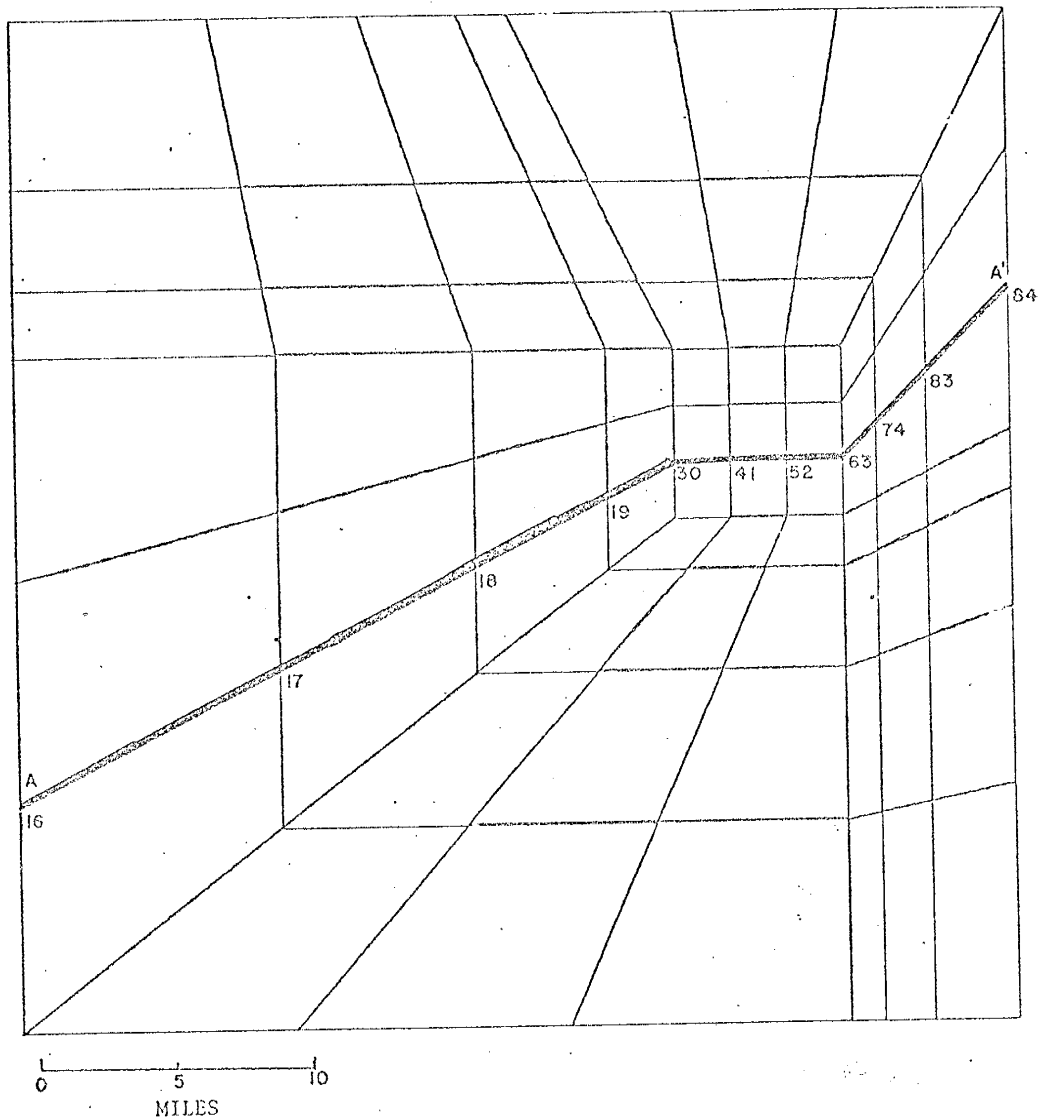
Fig. 22   Diagram of the cross section used in the plot of
concentration at the indicated nodal locations
shown in Figs. 23 and 24.

(a)

- @ 4,000 years
- x @ 16,000 years
- + @ 32,000 years

Horizontal Distance x 10^{-3} (ft)

(b)

- @ 4,000 years
- x @ 16,000 years
- + @ 32,000 years

Horizontal Distance x 10^{-3}
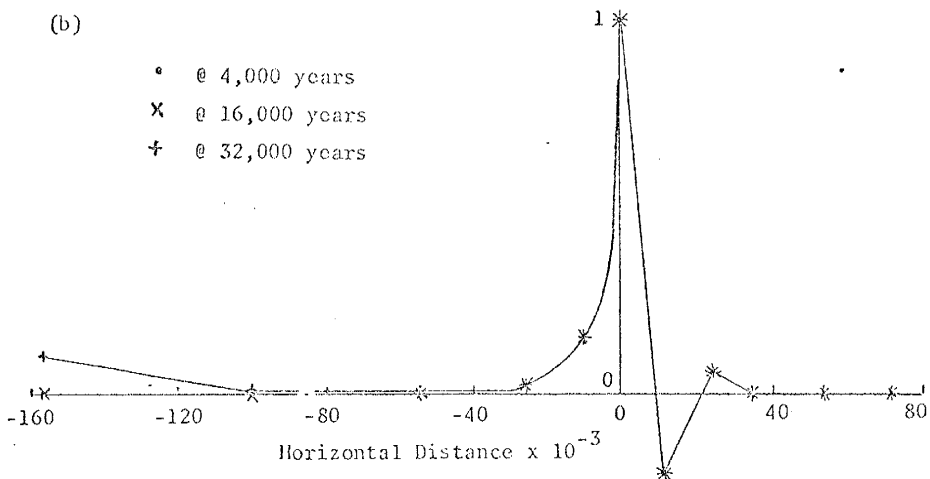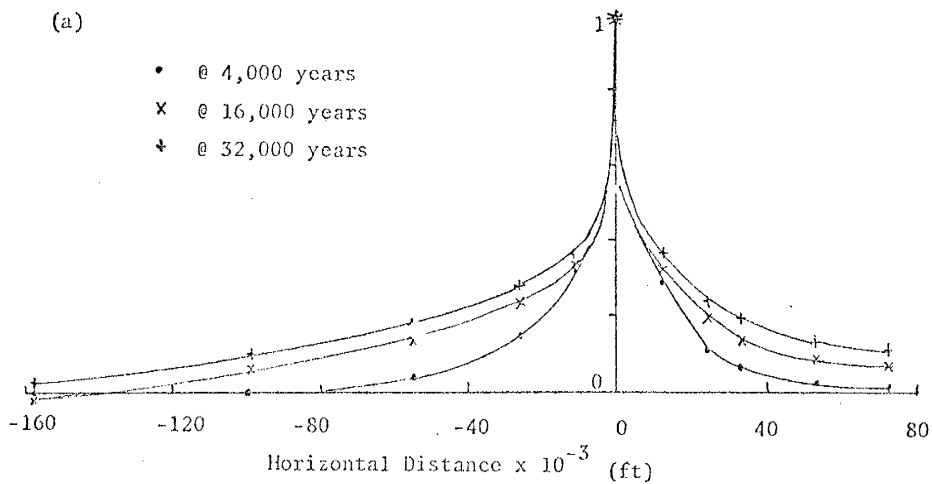
Fig. 23 Plots of normalized concentration at times of 4,000, 16,000, and 32,000 years along the cross section shown in Fig. 22 for dispersivities of (a) 24,000 feet and (b) 2,400 feet. Note that the origin of the ordinant is the injection well located at node 41.

• = 4,000 years

x = 16,000 years

1

0

-160   -120   -80   -40   0   40   80

Horizontal distance x 10^{-3}

Normalized concentration

-1

-2
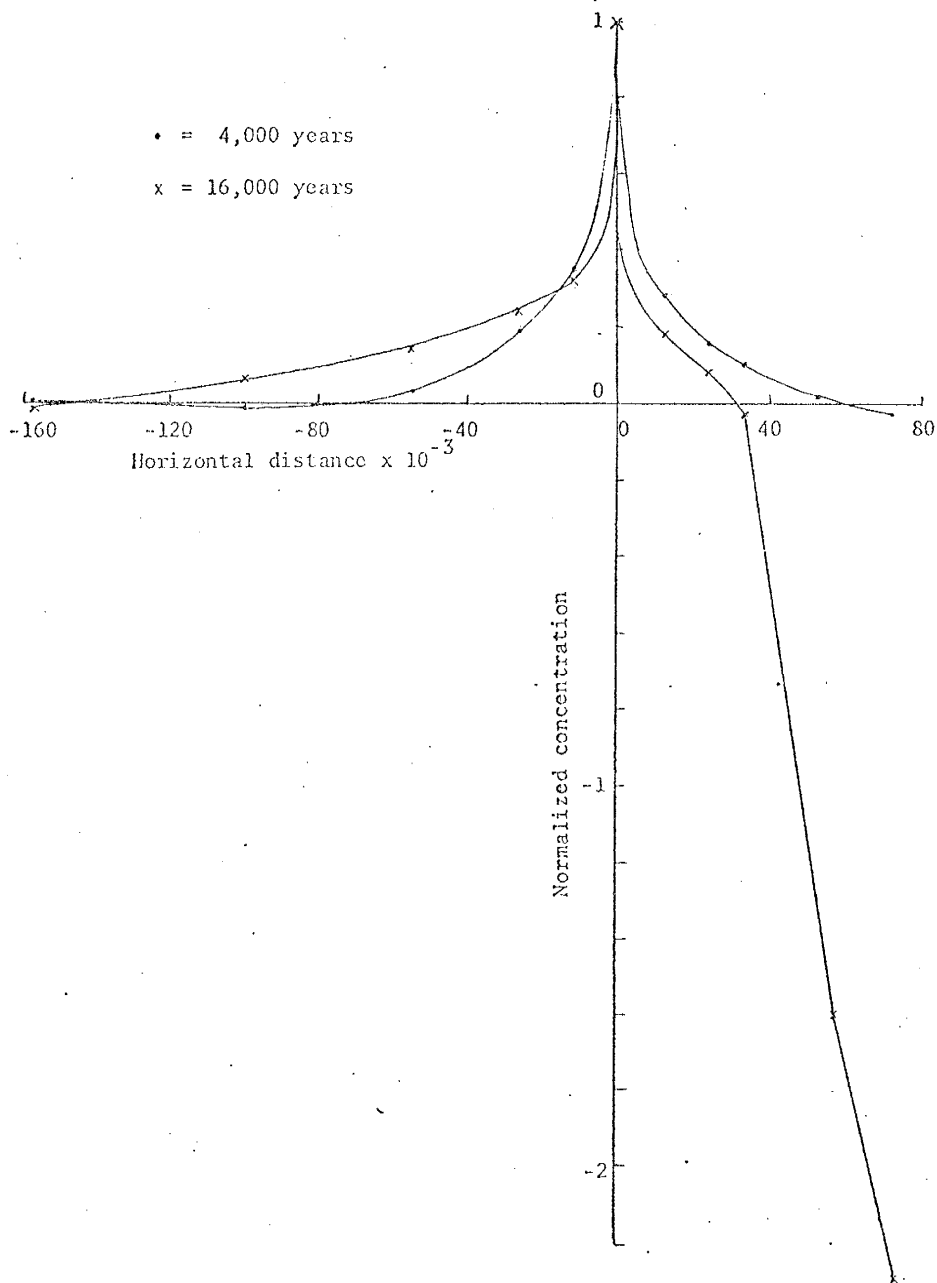
Fig. 24 Plots of normalized concentration at times of 4,000 and 16,000 along the cross section in Fig. 22 obtained by using a dispersivity of 2,400 feet and by using upstream weighting.

A -- Los Medanos
B -- Malaga Bend

0.2
0.1
0.05

0   5   10
MILES

Fig. 26 Normalized concentration contours at
t = 16,000 years and dispersivity = 300
feet, using irregular mesh and Galerkin
approach.

A -- Los Medanos
B -- Malaga Bend

A
0.2
0.1
0.05

0   5   10
MILES
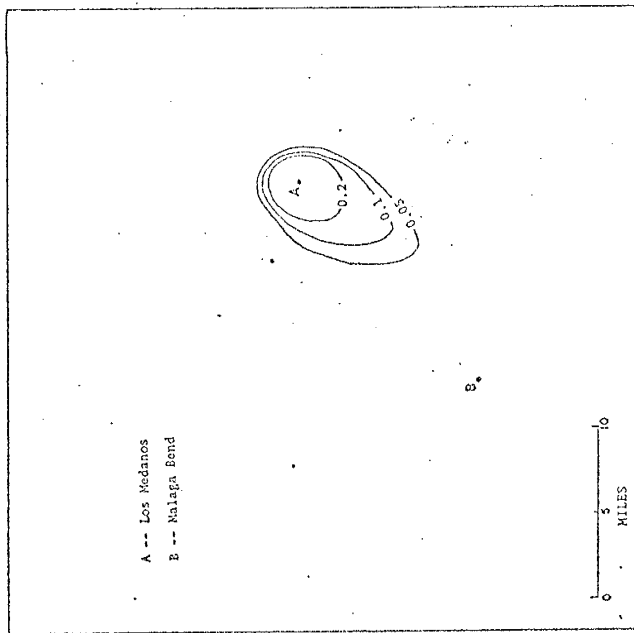
Fig. 25 Normalized concentration contours at
t = 4,000 years, dispersivity = 300
feet, using irregular mesh and Galerkin
approach.
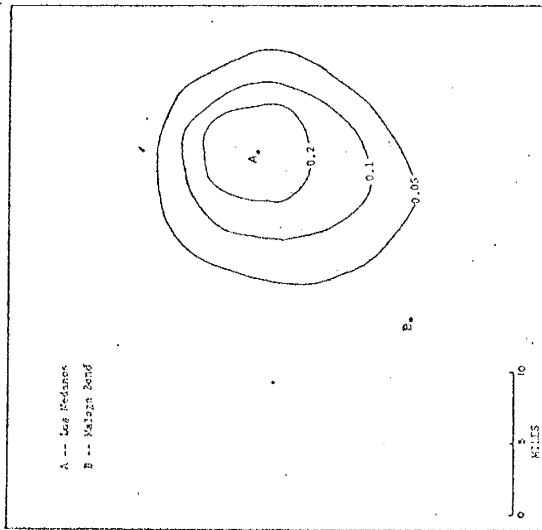
Fig. 27 Normalized concentration contours at t = 4,000 years, dispersivity = 24,000 feet, using irregular mesh and the Galerkin approach.
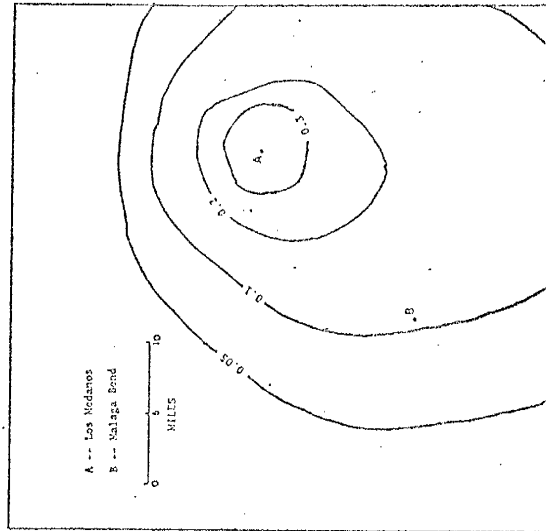
Fig. 28 Normalized concentration contours at t = 16,000 years, dispersivity = 24,000 feet, using irregular mesh and the Galerkin approach.
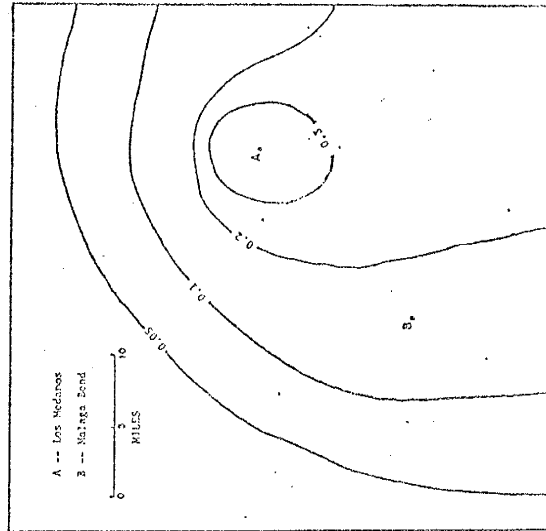
Fig. 29 Normalized concentration contours at t = 32,000 years, dispersivity = 24,000 feet, using irregular mesh and the Galerkin approach.

A -- Los Medanos
B -- Malaga Bend

A -- Los Medanos
B -- Malaga Bend

0   5   10
   MILES

0   5   10
   MILES

0   5   10
   MILES
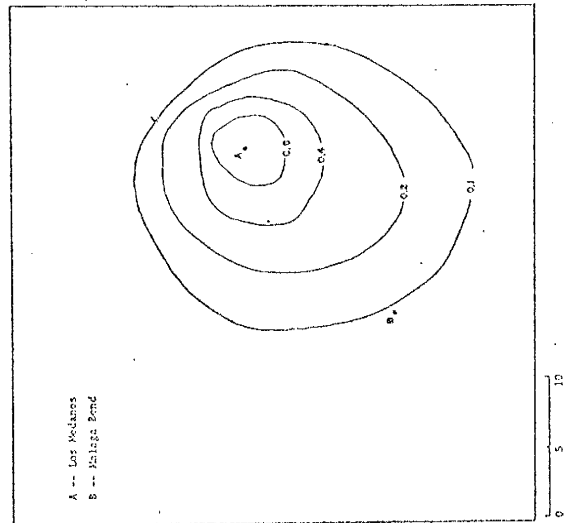
Fig. 33 Normalized concentration contours at
         t=4,000 years and dispersivity = 24,000
         feet, obtained using disturbed hydraulic
         head values, irregular mesh and the
         Galerkin approach.
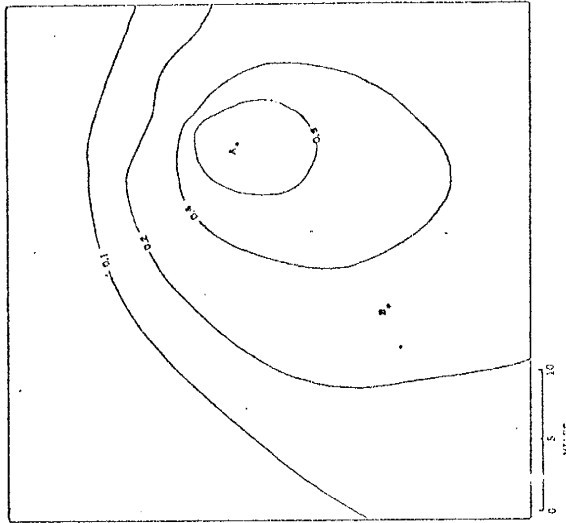
Fig. 34 Normalized concentration contours at
         t = 16,000 years and dispersivity =
         24,000 feet, obtained using disturbed
         hydraulic head values, irregular mesh
         and the Galerkin approach.
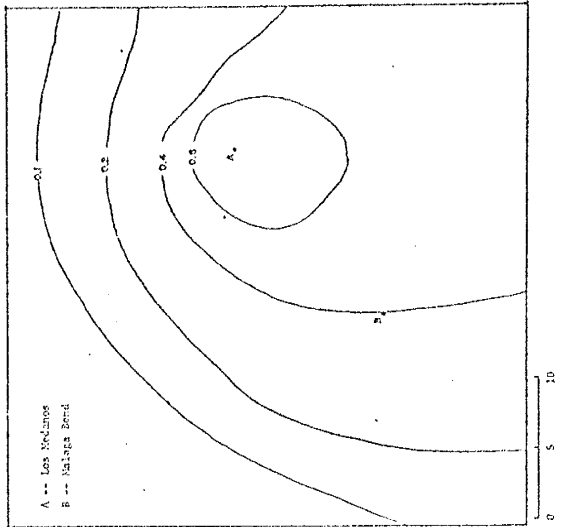
Fig. 35 Normalized concentration contours at
         t = 32,000 years and dispersivity =
         24,000 feet, obtained using disturbed
         hydraulic head values, irregular mesh
         and the Galerkin approach.
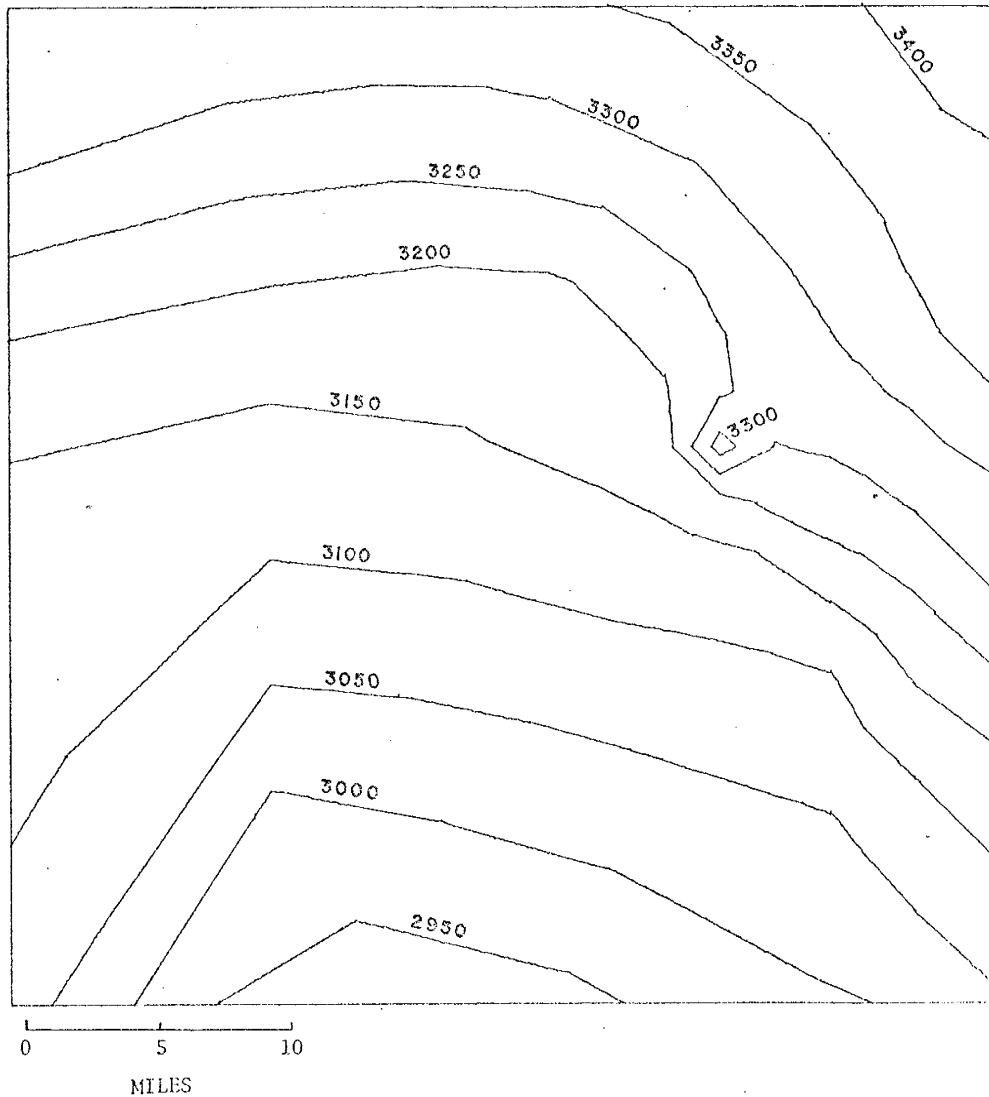
Fig. 30   Disturbed hydraulic head distribution obtained
by using the mesh in Fig. 18 and specifying
an incoming flux of 109,500 ft^3/year at node 41
along with the boundary hydraulic head values
obtained through interpolation from Fig. 14
Values are in feet.
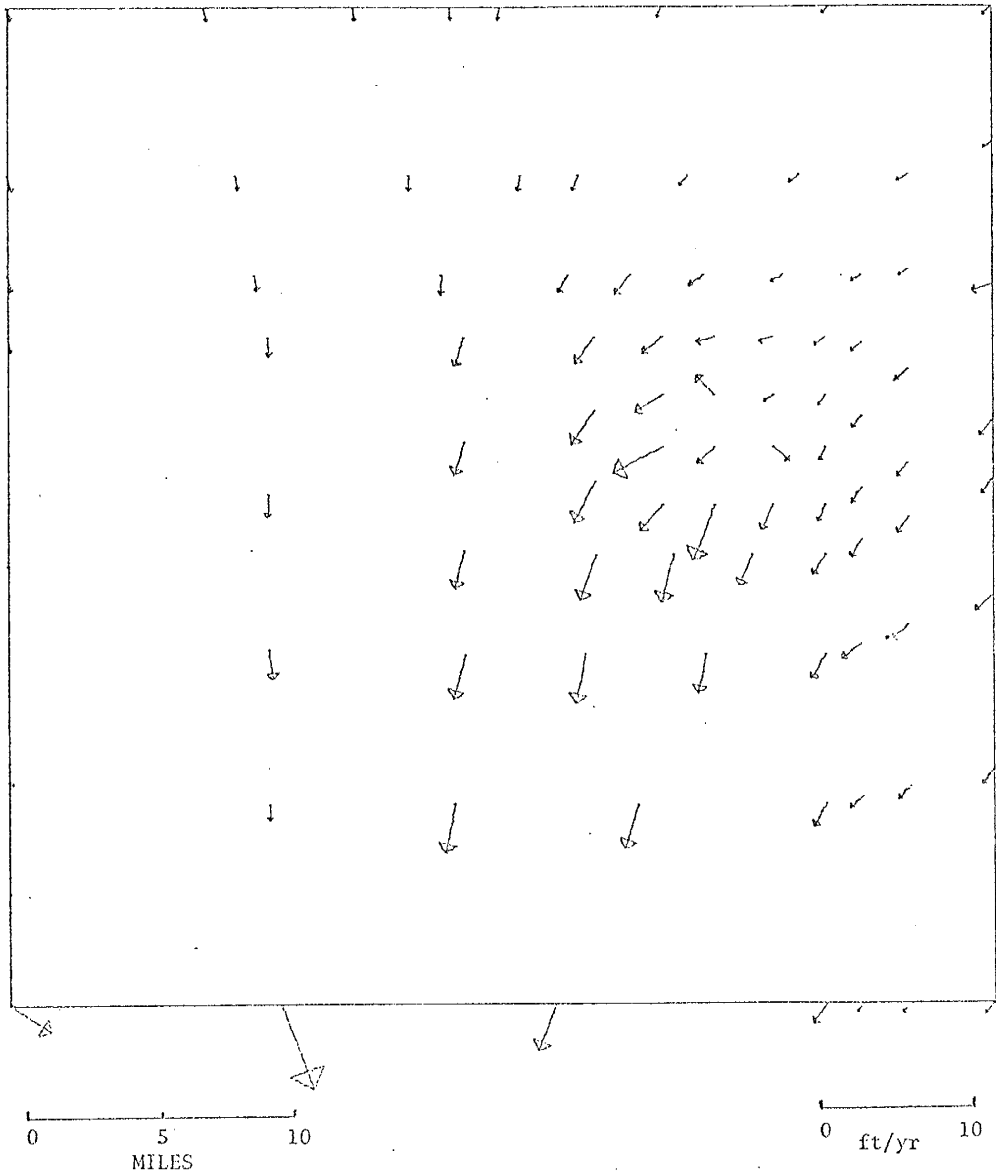
Fig. 31   Velocity distribution obtained from the irregular
mesh in Fig. 18   corresponding to disturbed
hydraulic potentials.
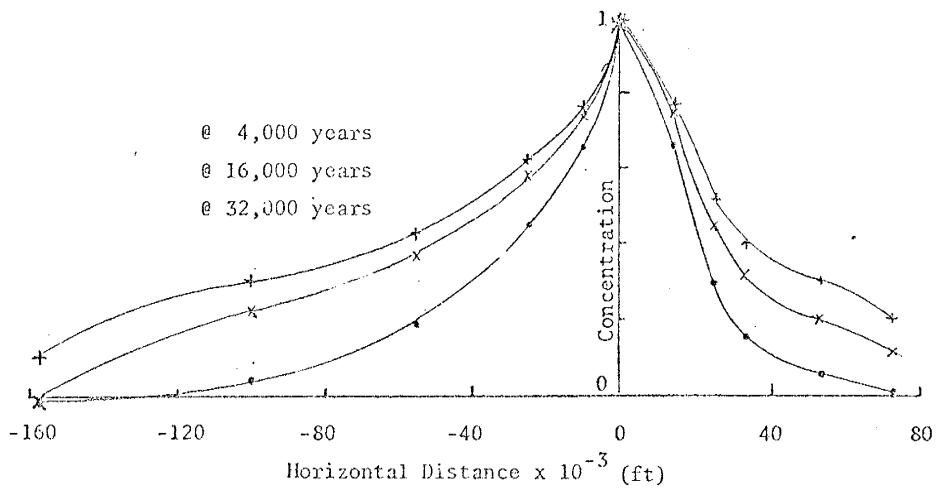
Fig. 32   Plots of normalized concentrations at times of
4,000, 16,000, and 32,000 years along the cross
section shown in Fig. 22   obtained using disturbed
hydraulic potentials and a dispersivity of 24,000
feet.

As a modification of the above problem, a steady-state contaminant injection rate of 109,500 ft^3/year (300 ft^3/day) was introduced at node 41 of Fig. 18. The effect of this nodal flux can be seen in the diagrams showing the disturbed hydraulic head contours and associated velocity distribution as seen in Figs. 30 and 31. The effect on contaminant concentration is a dramatic increase over the previous values obtained using undisturbed potentials (Figs. 32 through 35).

Although the 300 ft^3/day flow rate may be reasonable at early times, it is extremely doubtful that this flow rate would be maintained over the 32,000 year period of time used in these problems.

5.5.3. Two-dimensional transport using a regular, rectangular mesh

The preceding problem was successfully solved for a dispersivity of 300 feet using the regular, rectangular mesh of Figs. 36(a) and (b). The orientation of this mesh to irregular mesh of the preceding problem is shown in Fig. 37. The problem was run using undisturbed hydraulic head values and the distribution of these and their associated velocities is depicted in Figs. 38(a) and (b). The plot of the cross sectional normalized concentration in Fig. 39(a) shows the successful ellimination of numerical oscillation without the use of upstream weighting. Table 4 shows that little change occurs in the nodal normalized concentration values at times greater than 16,000 years.

Figs. 40(a) and (b) depict the advance of the concentration plume at times of 4,000 and 16,000 years. These figures correspond well with those of Figs. 25 and 26 where the irregular mesh was used. Neither of the two cases can be considered to accurately represent the real situation due to the distortion of the flow lines--i.e. the

direction of flow should be directly toward the Pecos River, whereas in this simulation, it is almost due south.

9	18	27	36	45	54	63	72	81	90	99
8	17	26	35	44	53	62	71	80	89	98
7	16	25	34	43	52	61	70	79	88	97
6	15	24	33	42	51	60	69	78	87	96
5	14	23	32	41	50	59	68	77	86	95
4	13	22	31	40	49	58	67	76	85	94
3	12	21	30	39	48	57	66	75	84	93
2	11	20	29	38	47	56	65	74	83	92
1	10	19	28	37	46	55	64	73	82	91

```
0            5            10
MILES
```

10.	20.	30.	40.	50.	60.	70.	80.	90.	100.	110.	120.
9.	19.	29.	39.	49.	59.	69.	79.	89.	99.	109.	119.
8.	18.	28.	38.	48.	58.	68.	78.	88.	98.	108.	118.
7.	17.	27.	37.	47.	57.	67.	77.	87.	97.	107.	117.
6.	16.	26.	36.	46.	56.	66.	76.	86.	96.	106.	116.
5.	15.	25.	35.	45.	55.	65.	75.	85.	95.	105.	115.
4.	14.	24.	34.	44.	54.	64.	74.	84.	94.	104.	114.
3.	13.	23	33.	43.	53.	63.	73.	83.	93.	103.	113.
2.	12.	22.	32.	42.	52.	62.	72.	82.	92.	102.	112.
1.	11.	21.	31.	41.	51.	61.	71.	81.	91.	101.	111.

Figs. 36 (a) Element and (b) node numbering schemes for
the problem involving 2-D flow using regular,
rectangular elements.

0   5   10

MILES
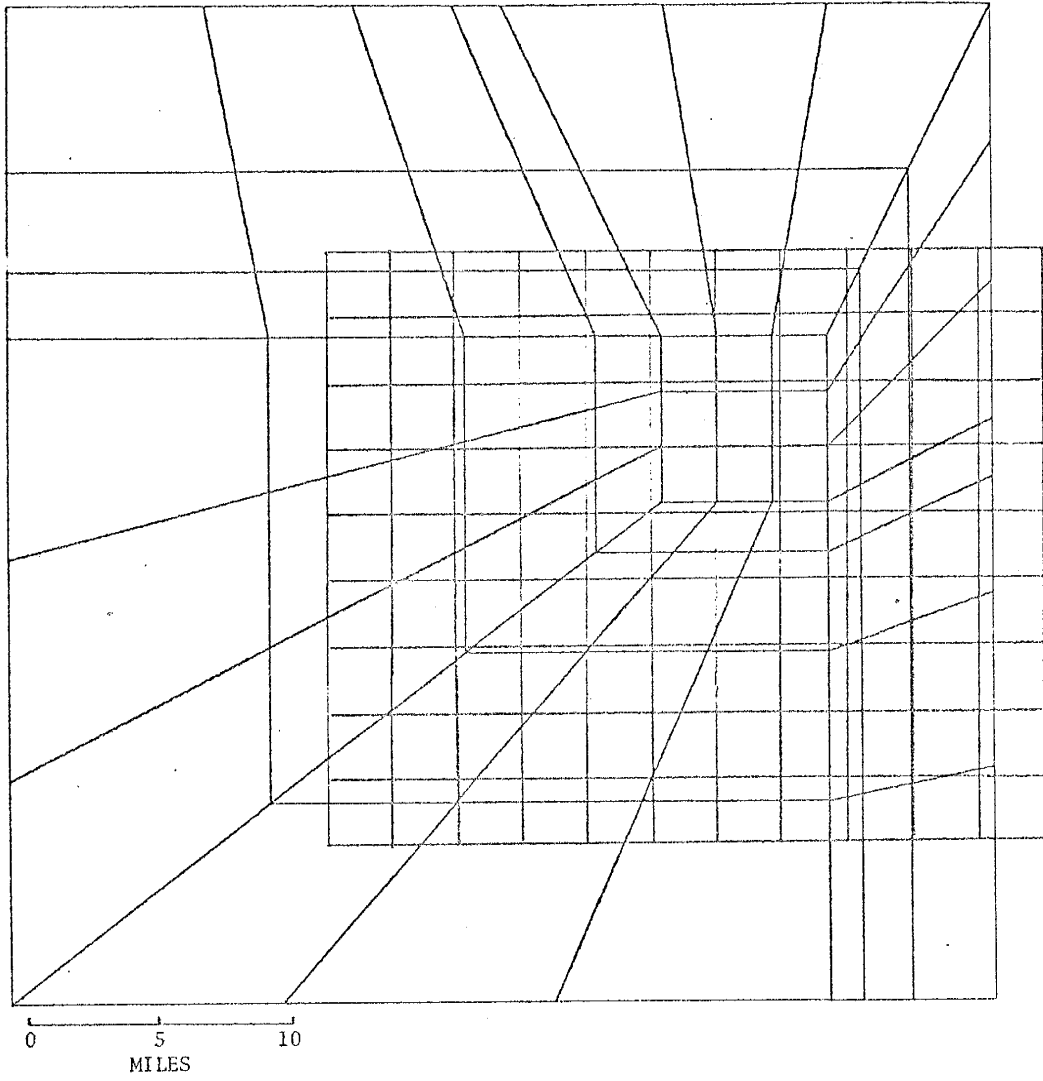
Fig. 37   Relationship of the regular rectangular mesh to the irregular mesh of Fig. 18 used for the two-dimensional flow problem.

(a)

A -- Los Medanos

B -- Malaga Bend

A₀

3350
3300
3250
3200
3150
3100
3050
3000
2950

B₀

(b)

0   ft/yr   10   0   5   10
                              MILES
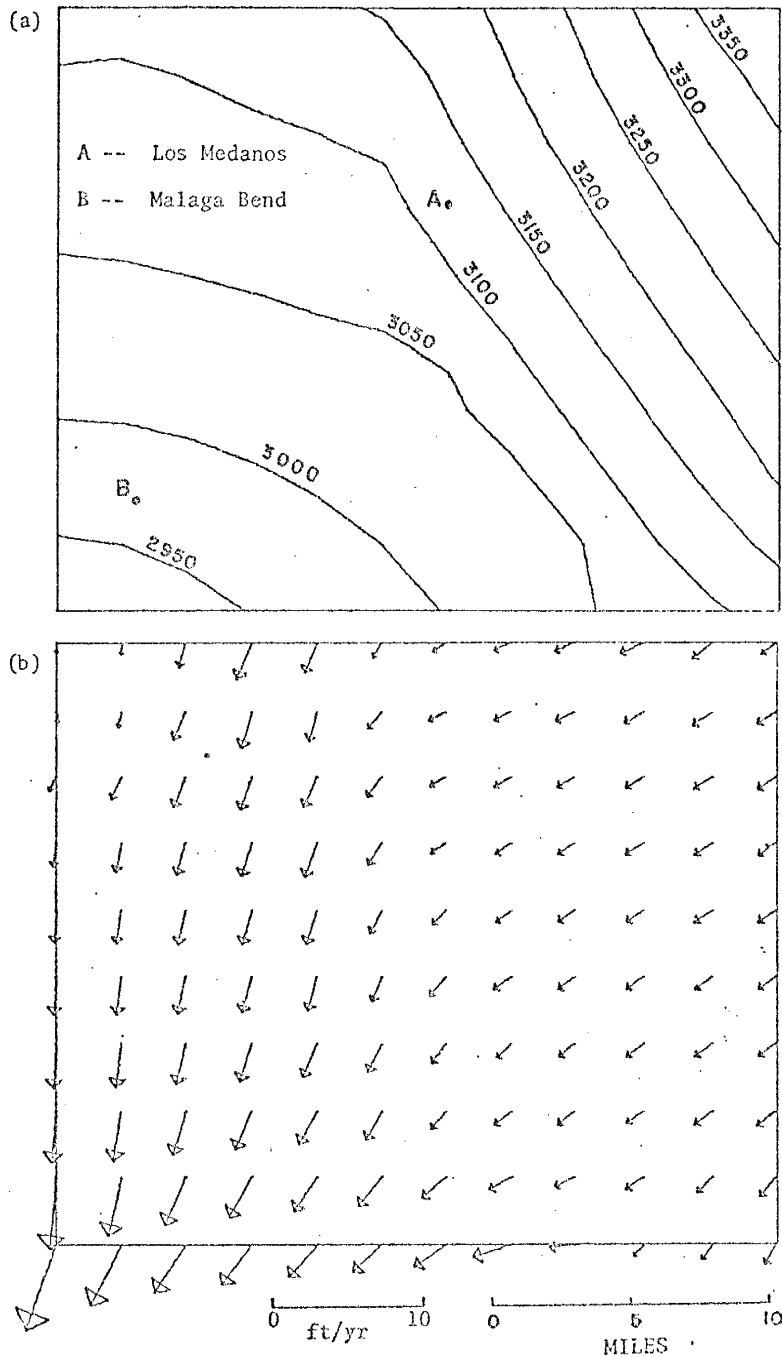
Fig. 38   Plots of (a) hydraulic head contours and (b)
           velocity distribution for the 2-D flow problem using
           the regular, rectangular mesh. Note that the
           distance scale is the same as for the irregular mesh.

Node number	Normalized nodal concentration value		
	4,000 years	16,000 years	32,000 years
1	-0.00002	0.02128	0.02683
12	0.00000	0.04370	0.04958
23	0.00006	0.07284	0.07740
34	0.01070	0.11624	0.11897
45	0.08047	0.19278	0.19410
56	0.29262	0.37046	0.37103
67	1.00000	1.00000	1.00000
78	0.02876	0.03017	0.03023
89	0.00156	0.00150	0.00152
100	0.00013	0.00013	0.00013

Table 4 Normalized concentration values obtained using the regular,
rectangular mesh at times of 4,000, 16,000, and 32,000 years
obtained using a dispersivity of 300 feet.
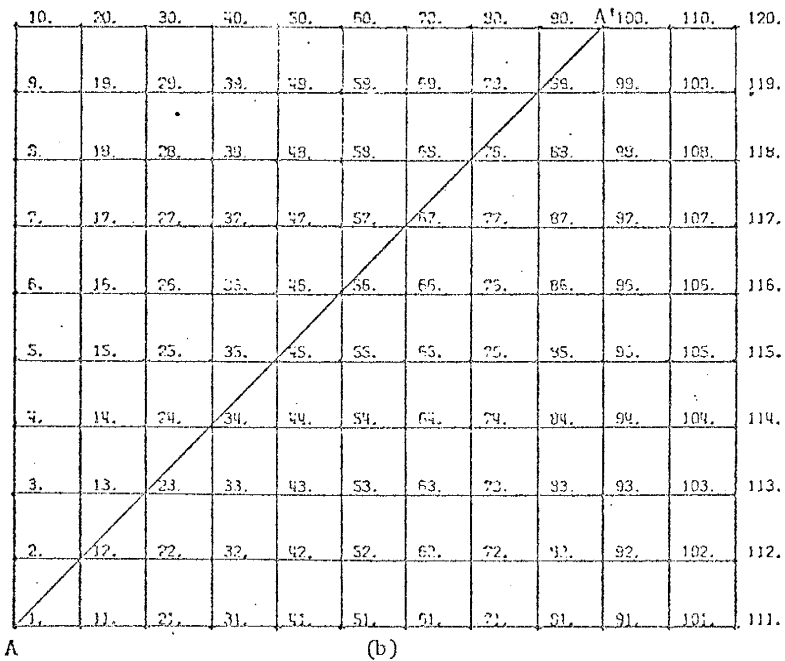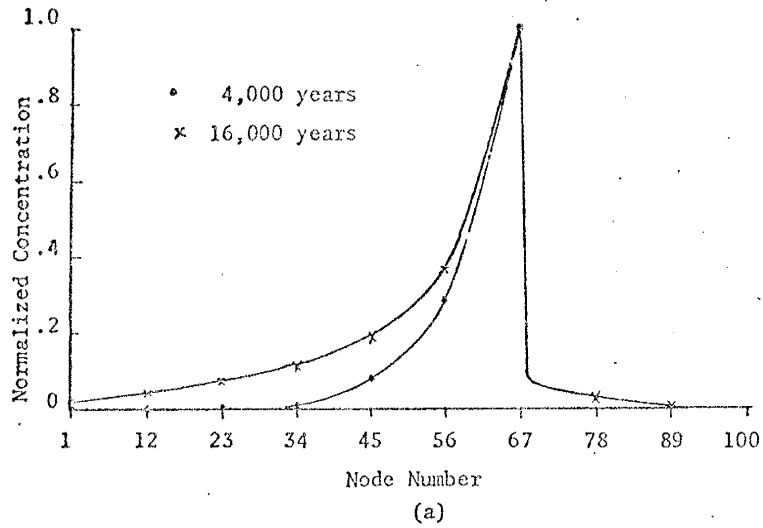
Fig. 39 (a) Plot of normalized concentration at corresponding equi-spaced nodal locations at times of 4000 and 16000 years. Node 67 corresponds to the injection point at Los Medanos. 300 ft. dispersivity.

(b) Cross section A-A' used to construct the above plot
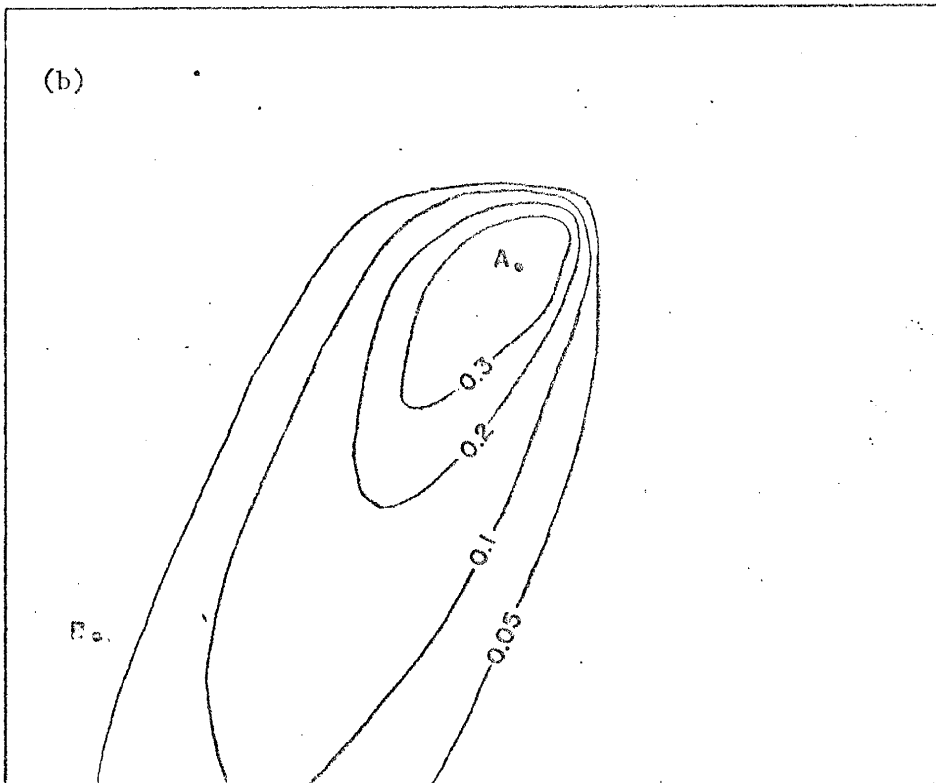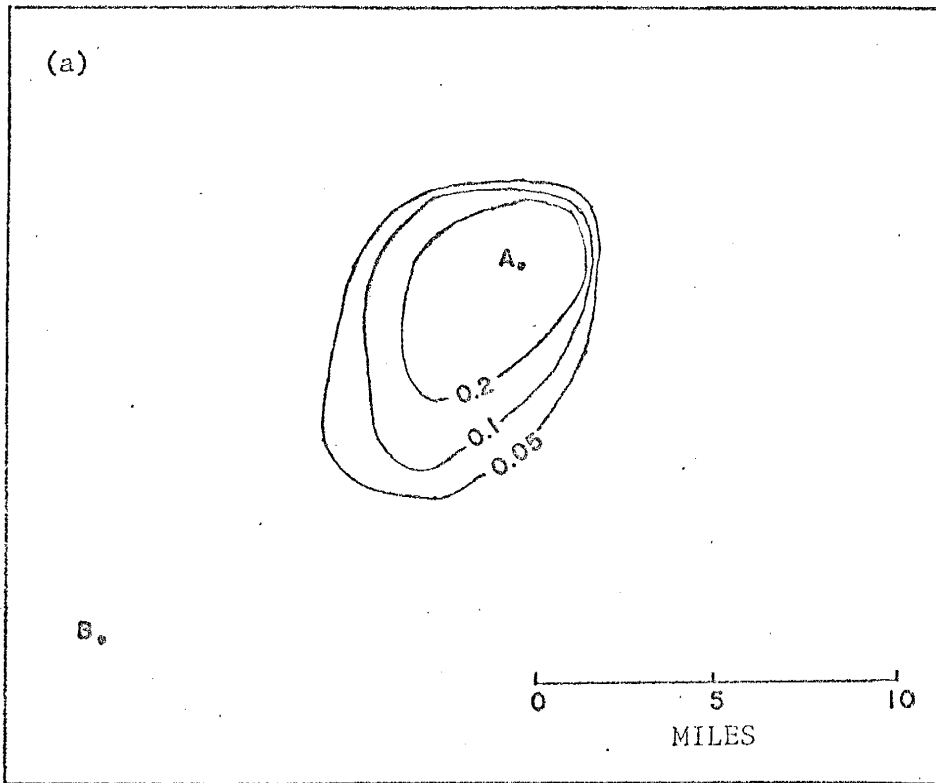
Fig. 40 Normalized concentration contours using regular,
rectangular mesh and upstream weighting functions
at (a) t = 4,000 years; and (b) t = 16,000 years.

6. Conclusions and Recommendations

Application of computer code, CLFEM5, to the sea water intrusion
problem revealed the following:

1) The results obtained for unsaturated intrusion were essentially
   identical to the published results of Huyakorn and Taylor (1977),
   which confirms the validity of the model for this type of problem.

2) The numerical oscillation encountered at the top nodal boundary
   due to the Peclet number of 10 could be effectively damped out by
   using upstream weighting functions.

3) The model gives essentially the same results for saturated and
   unsaturated solutions, independently of whether viscosity effects
   are taken into account.

Application of the numerical model to the transport problem in
the Los Medanos area problems revealed the following:

1) The one-dimensional analysis produced fairly close concentration
   front approximations to the analytical solutions. A slight bit
   of oscillation was detected using the dispersivity value of 300
   feet (Fig. 16(a)) but was not severe enough to warrant the use of
   upstream weighting functions.

2) The two-dimensional analysis using the irregular mesh produced
   numerical oscillation for dispersivities of 2,400 feet and less.
   Application of upstream weighting was unsuccessful in preventing
   this oscillation. Introduction of a flow rate of 300 ft^3/day
   at the borehole produced observable changes in the hydraulic
   head, velocity, and concentration distributions.

3) The problem of numerical oscillation was successfully overcome by
using a different mesh consisting of regular, rectangular elements.
Oscillation for the case of dispersivity equal to 300 feet was
successfully suppressed using this mesh.

Possible recommendations for future work might consist of: 1) de-
termination of the effect of the time increment selection on numerical
oscillation; 2) determination of the reason for the near steady-state
concentration results occuring for the later times in Table 4; 3) de-
termination of the reason for the deviation in flow direction in Figs.
21 and 38(b) as compared with that expected for Fig. 14; and 4) ap-
plication of the model to problems involving geothermal flow.

REFERENCES CITED

1. Bear, Jacob, 1972, Dynamics of fluids in porous media, American
    Elsevier Publication Co., New York, 764 p.

2. CRC Handbook of Chemistry and Physics, 1974, 55th ed.: Cleveland,
    Ohio, Chemical Rubber Company Press, p. D-224--D-225.

3. Domenico, P.A., and Palciauskas, V.V., 1973, Theoretical analysis
    of forced convective heat transfer in regional ground-water
    flow: Geol. Soc. of Amer. Bulletin, v. 84, p. 3803-3814.

4. Duguid, J. and Reeves, M., 1976, Material transport through porous
    media: a finite-element Galerkin model: Oak Ridge, Tennessee,
    Oak Ridge National Laboratory, ORNL 4928, 198 p.

5. Huyakorn, P.S., 1977, Solution of steady-state, convective trans-
    port equation using an upwind finite element scheme: Applied
    Mathematical Modeling, v.1, pp. 187-195.

6. Huyakorn, P.S., and Nilkuha, K., 1978, Solution of transient
    transport equation using an upstream finite element scheme:
    Applied Mathematical Modeling, in press.

7. Huyakorn, P.S., and Taylor, C., 1977, Finite element models for
    coupled groundwater flow and convective dispersion in Gray,
    W.G., and Pinder, G.F., eds., Finite elements in water resources:
    London, Pentech Press, p. 1.131-1.151.

8. International Critical Tables, 1929: New York, McGraw-Hill Book
    Co., v.5, pp. 12-15.

9. Lambert, Steven J., 1977, The geochemistry of Delaware Basin
    groundwaters: Albuquerque, New Mexico, Sandia Laboratories,
    SAND 77-0420, 13 p.

10. Lambert, S.J., and Mercer, J.W., 1977, Hydrologic inversigations of Los Medanos area, Southeastern New Mexico: Albuquerque, New Mexico, Sandia Laboratories, SAND 77-1401, 34 p.

11. Mercer, J.W., and Orr, B.R., 1977, Review and analysis of hydro-geologic conditions near the site of a potential nuclear-waste repository, Eddy and Lea Counties, New Mexico: U.S. Geological Survey Open File Report 77-123, Albuquerque, New Mexico, 35 p.

12. Pinder, G.F., 1973, A Galerkin-finite element simulation of ground-water contamination on Long Island, New York: Water Resources Research, v. 9, no. 6, pp. 1657-1669.

13. Pinder, G.F., and Gray, W.G., 1977, Finite element simulation in surface and subsurface hydrology, Academic Press, New York, 295 p.

14. Taylor, C., and Huyakorn, P., 1976, Finite element analysis of three-dimensional groundwater flow with convective dispersion in I.C.C.A.D. Second International Symposium on Finite Element Methods in Flow Problems: S. Margherita Ligure, Italy, June 14-18, 1976, Preprints, p. 565-579.

15. Witherspoon, P.A., Neuman, S.P., Sorey, M.L., and Lippmann, M.J., 1975, Modeling geothermal systems: International Meeting on Geothermal Phenomena and Its Applications, Rome, Italy, 1975, 68 p.

APPENDIX I

Computer Code CLFEM5 Data Input Instructions

Preparation of input data:

1. Problem card (I5)

   One card

   Col. 1-5   NPROB: Number of problems per run

2. Title card (20A4)

   One card

   Col. 1-80   TITLE: Title of problem

3. Control card (I5, 4F10.4, I5)

   One card

   Col. 1-5   NITMAX: Maximum no. of nonlinear iterations to be per-
                 formed

   6-15   ERROR: Prescribed tolerance ratio. Suggested value =
                 0.05 or 0.10

   16-25   RELAXF: Relaxation factor used to speed up convergence.
                 Normally set = 1 for conventional iteration;
                 less than 1 for under-relaxation; greater than
                 1 but less than 2 for over-relaxation.

   26-30   IMSHGN: Code for indicating if mesh data is to generated.
                 = 0 for no; =1 for yes. Mesh data may be auto-
                 matically generated if the domain is rectangular
                 in shape.

4. Control Card (16I5)

   Col. 1-5   NELEM: Total no. of elements

   6-10   NPOIN: Total no. of nodal points

Col. 11-15   NNE: No. of nodes per element

    16-20   NTYPE: Problem type (=1 for plane problem; = -1 for

              axisymmetric problem

    21-25   NDF: No. of degrees of freedom per node

    26-30   NDIM: No. of dimensions

    31-35   NMAT: No. of different materials

    36-40   NPROP: No. of material properties for each material set

    41-45   NTS: No. of time steps

    46-50   IDOUT: Code for specifying if discretization data is

              to be printed out (= 0 for no; = 1 for yes)

    51-55   IBREAD: Code for indicating if boundary node numbers

              are to be read in (= 0 for no; = 1 for yes)

    56-60   ISOLVR: Code for selecting the type of algebraic

              equation solver (= 1 for symmetric banded

              solver; = 2 for asymmetric banded solver)

    61-65   IDVAR: Code for indicating if dispersion coefficient

              depends on velocity (= 0 for no; = 1 for yes)

    66-70   JTST: Code for indicating which dependent variables

              are to be solved (= 1 means to determine the

              first dependent variable only or to determine

              both the first and second dependent variables;

              = 2 means to determine the second dependent

              variable only)

5. <u>Control card</u> (2I5, 4F10.4, 3I5)

One card

Col. 1-5   NONU: Number of nodes where initial values differ from

              default values

Col. 6-10   NSTEP: Code for controlling printout of computed nodal

                values. When NSTE` = n, results are printed out

                at each nth time step.

11-20   TIN: Size of first time increment

21-30   TMUL: Time multiplier

31-40   TMAX: Maximum value of time increment

41-50   THETA: Time weighting factor. For steady state problems,

                THETA = 1; for transient problems, THETA = 1.0

                and THETA = 0.5 correspond to backward and cen-

                tral time stepping respectively.

51-55   IVEL: Code for specifying if velocity computations and

                printout are required

56-60   IPLOT: Code for specifying if control plotting data

                are to be printed out for use in TPLOT1.FOR

61-65   JT: Dependent variable number for which gradients are

                required (= 1 for first dependent variable;

                = 2 for second dependent variable)

6. Weighting function parameter card (2I5, 4F10.3)

One card

Col. 1-5   IUPWIN: Code for indicating if upstream weighting

                functions are to be employed (= 0 for no;

                = 1 for yes)

6-10   ICAL: Code for indicating if weighting factors are to

                be calculated (= 0 for no; = 1 for yes)

11-20   WFAC: Default value of weighting factor in x-direction

21-30   YFAC: Default value of weighting factor in y-direction

31-40   VCX: Default value of velocity component in x-direction

41-50   VCY: Default value of velocity component in y-direction

7. Plotting control card (I5, 4F10.4)

*** To be omitted if (IPLOT.EQ.0)

One card

Col. 1-5   NCL: Number of contour lines

     6-15   HO: Maximum value of function to be plotted

     16-25   HW: Minimum value of function to be plotted

8. Plotting parameter card (8F10.4)

*** To be omitted if (IPLOT. EQ. 0)

One card

Col. 1-10   DXSCL: Scale in x-direction in actual units per inch

    11-20   DYSCL: Scale in y-direction in actual units per inch

    21-30   XMIN: Minimum value on x axis

    31-40   YMIN: Minimum value on y axis

9. Default initial value card (8F10.4)

One card

Col. 1-10   HINV(1): Default initial value of the first dependent

                       variable

    11-20   HINV(2): Default initial value of the second dependent

                       variable

10. Material property index card(s) (16I5)

*** To be omitted if NMAT = 1

No. of cards = NELEM/16 + (1 or 0)

Col. 1-5   IPROP(1) to IPROP(NELEM) = Material number(s) of first

    6-10   through last elements

    etc.

11. Material property card(s) (8E10.3)

   This card set is to be prepared for each material. Number of cards in

   each set = NPROP/8 + (1 or 0)

   Col. 1-10   PROP(I,1): First property belonging to material no. I

       11-20   PROP(I,2): Second property belonging to material no. I

       etc.

12. Mesh parameter card (2I5, 2F10.3)

   *** This card type is to be omitted when IMSHGN = 0.

   One card

   Col. 1-5   NROWS: Number of rows in the mesh

       6-10   NCOLS: Number of columns in the mesh

       11-20   DXMAX: Maximum value of spatial increment allowed in

                        the x-direction

       21-30   DYMAX: Maximum value of spatial increment allowed

                        in the y-direction

13. Mesh parameter card (8F10.3)

   *** This card type is to be omitted when IMSHGN = 0

   One card

   Col. 1-10   DX: Delta-x of the first block

       11-20   DY: Delta-y of the first block

       21-30   XO: Maximum value of x-coordinate in the domain

       31-40   YO: Maximum value of y-coordinate in the domain

       41-50   SCFX: Scale factor in the x-direction

       51-60   SCFY: Scale factor in the y-direction

       61-70   XSTART: Minimum x-coordinate in the domain

       71-80   YSTART: Minimum y-coordinate in the domain

14. <u>Coordinate cards</u> (I5, 4F10.4)

   *** This card type is to be omitted when IMSHGN = 1

   Total no. of cards = NPOIN

   Col. 1-5   N: Node number

       6-15   CORD(N,1): X-coordinate of node number N

      16-25   CORD(N,2): Y-coordinate of node number N

15. <u>Element connection cards</u> (16I5)

   *** This card type is to be omitted when IMSHGN = 1

   No. of cards = NELEM

   Col. 1-5   N: Node number

       6-10   LNODS(N,J): Nodal connections of element no. N

     11-15   etc.

16. <u>First type boundary value control card</u> (I5)

   Col. 1-5   NB: Total no. of prescribed boundary values of the

                      unknown functions (first type boundary condition)

17. <u>First type boundary value card(s)</u> (2I5,2F10.5)

   No. of cards = NB

   Col. 1-5   NDNO: Node number

       6-10   MDEG: Dependent variable number

     11-20   VALV(I): Prescribed value of unknown function

18. <u>Second type boundary value control card</u> (I5)

   One card

   Col. 1-5   NDFLUX: Total number of prescribed normal flux values

19. <u>Second type boundary value card(s)</u> (2I5, 2F10.5)

   *** To be omitted if NDFLUX = 0

   No. of cards = NDFLUX

Col. 1-5   NDNO: Node number

　　6-10   MDEG: Dependent variable number

　　11-20   FLVAL(I): Prescribed flux value

20. <u>Initial value card(s)</u> (I5, 2F10.4)

*** To be omitted if NONU = 0

No. of cards = NONU

Col. 1-5   N: Node number

　　6-15   HINT(N,1): Initial value of first variable

　　16-25   HINT(N,2): Initial value of second variable

Property values for the contamination transport problem:

1. <u>h-c model</u>

   PROP(K,1): Hydraulic conductivity in x-direction or K_o/U

   PROP(K,2): Hydraulic conductivity in y-direction or K_o/U

   PROP(K,3): Storage coefficient of aquifer

   PROP(K,4): Negative of density difference ratio, $-\varepsilon$

   PROP(K,5): Set equal to zero

   PROP(K,6): Set equal to unity

   PROP(K,7): Set equal to unity or $U_o d/D_o$

   PROP(K,8): Dispersion coefficient D_x or D_x/D_o; for IDVAR = 1, this denotes dispersivity factor.

   PROP(K,9): Dispersion coefficient D_y or D_y/D_o; for IDVAR = 1, this denotes dispersivity factor.

   PROP(K,10): Maximum solute concentration in say gm/liter

   PROP(K,11): Minimum solute concentration in say gm/liter

   PROP(K,12): set equal to zero for steady state case

*** Note: For the transient case, PROP(K,12) = the porosity of porous medium.

2. <u>ψ-c model</u>

   PROP(K,1): Set equal to unity

   PROP(K,2): Set equal to unity

   PROP(K,3): Set to zero

   PROP(K,4): Density difference ratio, ε

   PROP(K,5): Set equal to zero

   PROP(K,6): Set equal to unity

   PROP(K,7): Set equal to unity or Ud/D_o

   PROP(K,8): Dispersion coefficient D_x or D_x/D_o

PROP(K,8): Dispersion coefficient D_x or D_x/D_o

PROP(K,9): Dispersion coefficient D_y or D_y/D_o

For IDVAR = 1, PROP(K,8) and PROP(K,9) denote dispersivity factors.

PROP(K,10): Set equal to zero

PROP(K,11): Set equal to zero

PROP(K,12): Set equal to zero

APPENDIX II

Outline of Problems Run Using CLFEM5

I. Sea water intrusion, $Pe = 10$ (using the graded mesh of Fig. 4)

    A. Unsaturated salt water ($\varepsilon = 0.025$; $K_o = 150$); without viscosity effects (i.e. earlier version of CLFEM5); without using upstream weighting.

    B. Unsaturated salt water with viscosity effects; unweighted.

    C. Saturated salt water ($\varepsilon = 0.198$; $K_o = 19.2$); without viscosity effects; unweighted.

    D. Saturated salt water with viscosity effects; unweighted.

    E. Unsaturated salt water without viscosity effects; using asymmetric weighting functions.

II. One-dimensional transient transport (equal time steps of 250 years adding up to 10,000 years) in Los Medanos area (divided into 40 uniform rectangular elements, 2,350 feet by 1,000 feet; 82 nodes); the hydraulic head boundary condition values were specified as 3,150 feet at nodes 1 and 2 (at Los Medanos); 3,083 feet at nodes 13 and 14 (14,100 feet southwest of Los Medanos on the cross section in Fig. 15); and 2,930 feet at nodes 81 and 82 (at Malaga Bend). Hydraulic conductivity values were specified as shown in Fig. 15. The following cases were run:

    A. Dispersivities in Zones 1 and 2 (Fig. 15) were set equal to 300 feet.

    B. The dispersivity in Zone 1 was set equal to 300 feet; the

dipersivity in Zone 2 was set equal to 1,200 feet.

III. Two-dimensional transient transport (equal time steps of 800
   years adding up to 32,000 years) in Los Medanos area (using the
   irregular mesh in Fig. 18); the initial hydraulic head boundary
   conditions were specified on the outside nodes of Fig. 18 using
   interpolated head values form Fig. 14; hydraulic conductivities were
   specified as shown in Fig. 15. The following cases were run:

   A. Longitudinal and transverse dispersivities were uniformly set
      over the entire region in Fig. 15 as 1) 300 feet; 2) 2,400 feet;
      and 3) 24,000 feet. The fluid flux boundary condition at the well
      (Node 41) was specified as 0 ft^3/yr. No upstream weighting was
      used.

   B. Longitudinal and transverse dispersivities were set at 2,400
      feet; the fluid flux boundary condition at the well was set at
      0 ft^3/yr; and upstream weighting was used.

   C. Longitudinal and transverse dispersivities were set at 24,000 feet;
      the fluid flux boundary condition at the well was set at 109,500
      ft^3/year (300 ft^3/day); and no upstream weighting was used.

IV. Two-dimensional transport (equal time steps of 400 years adding up
   to 24,000 years followed by equal time steps of 1,000 years adding
   up to 64,000 years) in Los Medanos area (using the regular, rectang-
   ular mesh of Fig. 36); hydraulic head values were specified using
   interpolated head values from Fig. 14; hydraulic conductivites were
   specified using the division shown in Fig. 15. The following cases
   were run:

A. Longitudinal and transverse dispersivities were uniformly set over the entire area as 300 feet. The problem was run:

1) without using upstream weighting;

2) with upstream weighting applied.

This thesis is accepted on behalf of the faculty of the

Institute by the following committee:

Allan F. Mützelburg

Lynn W. Melton

P. Huyakorn

Date _12/7/78_